Investigation of Secondary Hardening in Co–35Ni–20Cr–10Mo Alloy Using Analytical Scanning Transmission Electron Microscopy

A THESIS
SUBMITTED TO THE FACULTY OF
UNIVERSITY OF MINNESOTA
BY

Daniel David Sorensen

IN PARTIAL FULFILLMENT OF THE REQUIREMENTS
FOR THE DEGREE OF
MASTER OF SCIENCE

William W. Gerberich, K. Andre Mkhoyan

August 2014

Acknowledgements

I would like to thank my advisors Professor William Gerberich and Professor Andre Mkhoyan for their support, guidance, and patience through my graduate career. I was very fortunate to have a co-advising team that not only helped with my research, but allowed me to learn and grow as a scientist in ways I never imagined. I would like to extend a special thank you to my industry advisor Dr. Bernie Li who has been a mentor to me since my internship in 2005. Dr. Li has been there for guidance, support, and practical experimental feedback and knowledge. I would also like to acknowledge the Medtronic Neuromodulation management for their monetary and moral support of this research.

I would also like to acknowledge a number of key research collaborators whom without their guidance, thoughtful discussions, help, tough love, or combination of all, this research would not have been possible. Dr. Ozan Ugurlu and Dr. Jason Myers for their near infinite patience as I was learning to operate the electron microscopes and interpret data they produced. I truly cannot thank you enough. Mr. Kevin Roberts at the Minnesota Nano Center for teaching me how to operate a dual beam FIB and prepare high quality TEM lamella. Dr. Doug Stauffer for his mentorship, lessons on micro and nano mechanics, and helpful conversations. I would also like to acknowledge the Gerberich and Mkhoyan groups for their support, training, and helpful conversations with special thanks to Dr. Jong Seok Jeong, Dr. Aloysius Gunawan**,** Andrew Wagner, and Michael Odlyzko. Special thanks to Eric Hintsala for careful proofreading of this manuscript. I would also like to thank my colleagues at Medtronic for their moral and technical support especially Dr. Bill Wolf and Dr. Jason Heffelfinger for introducing me to the discipline of materials science and electron microscopy in 2001, Bruce Peacock for thoughtful discussions and support, Margaret Bush for helpful discussions and careful proofreading of this manuscript, and Josh Casey and Dr. Mallika Kamarajugadda for their mentorship over the years.

Last and certainly not least, I would like to thank my friends and family for their support.

Dedication

This thesis is dedicated to my parents Dave and Geri Sorensen, my wife Melissa, and our wonderful son Ryan all of whom are a constant source of inspiration.

Abstract

The mechanism of secondary hardening in MP35N (Co–35Ni–20Cr–10Mo) alloy due to exposures at elevated temperatures has been studied. It was observed that short exposure to elevated temperatures increased the ultimate tensile strength and yield stress while decreasing the elongation of MP35N wires. Upon aging at temperatures from 300°C to 900°C the elastic modulus increased although no changes in crystallographic orientation or microstructure were observed. No proposed model for this apparent increase in elastic modulus is suggested as yet. The grain size and major texture components were unchanged following aging. Analytical scanning transmission electron microscope investigation showed that MP35N is hardened by preferential segregation of molybdenum to stacking faults and deformation twins. It also revealed that the concentration of molybdenum segregation was proportional to the amount of initial cold work before aging.

List of Abbreviations

MP35N – Multi-Phase 35% Nickel, trade name for Co-35Ni-20Cr-10Mo Alloy

FCC – Face Centered Cubic

HCP – Hexagonal Close Packed

SFE – Stacking Fault Energy

TEM – Transmission Electron Microscopy

SAD – Selected Area Diffraction

ETFE – Ethylene Tetrafluoroethylene

PTFE – Polytetrafluoroethylene

SEM – Scanning Electron Microscope

EBSD – Electron Backscatter Diffraction

TEM – Transmission Electron Microscope

BF-TEM – Bright Field Transmission Electron Microscopy

DF-TEM – Dark Field Transmission Electron Microscopy

WBDF – Weak Beam Dark Field

SAD – Selected Area Diffraction

EFTEM – Energy Filtered Transmission Electron Microscopy

EELS – Electron Energy Loss Spectroscopy

STEM – Scanning Transmission Electron Microscopy

HAADF – High Angle Annular Dark Field

EDS – Energy Dispersive Spectroscopy

Table of Contents

LIST OF TABLES

LIST OF FIGURES

1 BACKGROUND

1.1 INTRODUCTION

This work will discuss the phase transformations that occur in Multi-Phase 35% Nickel (MP35N, Co-35Ni-20Cr-10Mo) alloy as a result of aging cycles at various times and temperatures. MP35N was developed as a family of Co-Ni based alloys in 1968 by G.D. Smith [1]. MP35N was originally used for bolts and fasteners due to its high strength, ductility, fracture toughness, and corrosion resistance [2]. After years of use in large scale applications the medical device industry began using the high strength, ductility, and biocompatibility of MP35N to create conductor coils and cables for cardiac stimulation and neuromodulation devices [3-5].

1.1.1 MOTIVATION

MP35N has been historically used in applications requiring high strength, ductility, and fracture toughness such as bolts, fasteners, and plates. The macroscopic size of the material in these traditional uses resulted in research being performed on large “bulk” samples with aggressive amounts of cold work, high heat treatment temperatures, and aging times on the order of hours. The medical device industry commonly uses cold drawn MP35N wires as conductor coils and cables in leads for pacing and neuromodulation [3-5]. The wires used for this application range from 0.001 inch -0.004 inch (25 μm to 102 μm) in diameter, experience aging temperatures ranging from 100°C to 900°C, and aging times on the order of seconds to minutes. While these conditions would have a negligible effect on MP35N components with large geometries they have an appreciable effect on the mechanical properties and fatigue life of the fine wires that are used to deliver therapy. The current literature on the relationships between

microstructure and mechanical properties in MP35N, while thorough for previous uses of MP35N, had not taken into account how the material behaves on the “meso” scale. This thesis will discuss the relationship between microstructure and mechanical relationship for MP35N fine wires with lower amounts of cold work (<70% cold work) and low processing temperatures to better approximate the conditions medical device MP35N wire experiences during processing.

1.2 THE PRIMARY STRENGTHENING MECHANISM IN MP35N

MP35N was developed in 1968 as part of a family of cobalt based super alloys with a single phase γ (fcc) structure. Upon the addition of cold work the yield strength of the material was found to increase by up to a factor of five [6]. Transmission electron microscopy and x-ray diffraction studies reported the presence of thin platelets with a hexagonal structure. Further diffraction experiments indicated the platelets had an orientation relationship with the matrix of (0001)ε//(111)γ [7]. “Multiphase” alloys with Co:Ni ratios greater than 45:25 showed evidence of strengthening by the formation of stress induced hexagonal martensite plates (ε phase) as determined by integration of x-ray diffraction peaks [6]. This transformation was expected as the Multiphase family of alloys was created based on the γ→ε transformation observed in pure cobalt and Co-Ni binary alloys as shown in Figure 1.1.

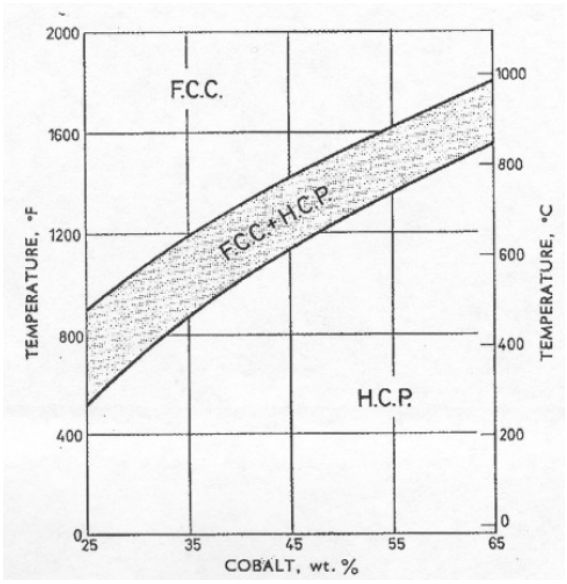

Figure 1.1 - Early phase diagram for Co-35Ni-20Cr-10Mo [7].

Experiments using alloys with Co:Ni ratios less than 45:25 were unable to resolve hexagonal martensite using x-ray diffraction. While the authors performed selected area electron diffraction studies and claimed to observe diffraction peaks from a hexagonal structure, the material analyzed was 80% cold rolled and the diffraction pattern showed evidence of severe amounts of deformation that could have resulted in resulted in significant smearing of the diffraction pattern and other artifacts which could then lead to errors in indexing. Image analysis was performed on a sample of 35Co:35Ni to determine the thickness and spacing of the platelets following cold rolling. The plates were measured to be 0.03 μm thick and spaced 0.14 μm apart [6].

A study by Drapier et al. [7] performed shortly after the initial work by Youngblood and Graham [6] investigated the primary mode of strengthening using x-ray and electron diffraction and again, identified coherent hexagonal martensite (ε) platelets forming on

{111} habit planes upon cold working [7]. The thin interlocking platelets observed in the fcc grains were hypothesized to be effective barriers to dislocation motion, thus a Hall-Petch type relationship was developed in which the yield strength was inversely proportional to the platelet spacing. (Figure 1.2) [7].

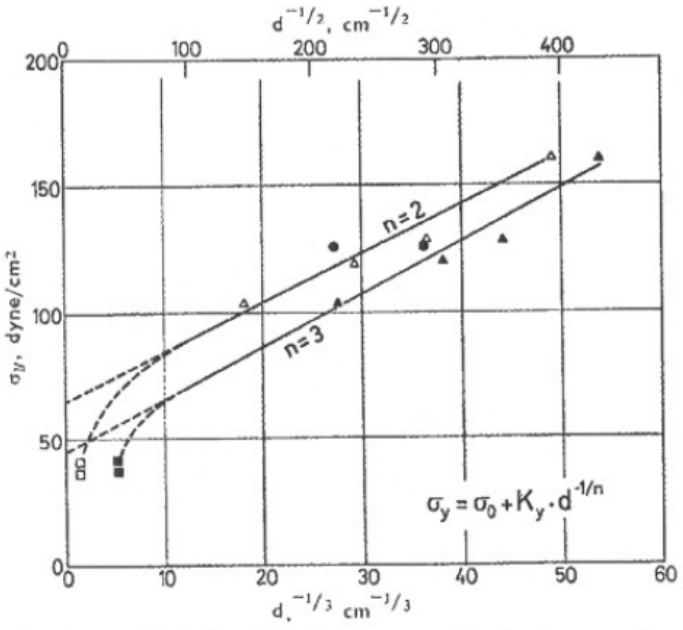

Figure 1.2 - Relationship between platelet spacing and yield strength of cold worked MP35N [7].

Fully annealed MP35N was also analyzed using transmission electron microscopy to examine the dislocation structure and measure the stacking fault energy (SFE). The SFE for material in the annealed condition was found to range from 26.2 to 28 erg/cm^2 [7].

Studies by Raghavan et al. [8] were the first to propose the plate-like features previously observed by Drapier et al. [7] and Graham et al. [6] were deformation twins instead of hexagonal martensite. In the study, three separate conditions of MP35N were analyzed; 59% cold worked, 59% cold worked + aging at 592°C for 4 hours, and 59% cold work + aging at 787°C for 4 hours. Investigation of the cold worked sample showed a

microstructure consisting of plates forming along {111} planes and diffraction analysis confirmed the plates were deformation twins [8] and not hexagonal martensite as previously reported. The study concluded that primary hardening was a result of deformation twinning and not the formation of stress induced martensite as previously reported [8].

Work performed by Singh and Doherty [9] addressed deformation twinning followed by secondary hardening upon aging as observed in MP35N. This is in contrast to low temperature recrystallization as found in 70-30 brass, another low stacking fault energy alloy. Their investigation utilized three different processing histories of MP35N: fully annealed, 48% cold drawn, and 53% cold drawn. The results of this study showed primary hardening in MP35N to be a direct result of traditional work hardening, but at high strains or stresses the formation of plate like features along the (111) planes were observed (Figure 1.3). These plates were determined to be both deformation twins and hexagonal martensite by careful electron diffraction studies with the possibility of hexagonal martensite spots were formed by double diffraction. Further diffraction studies on fine grained 60% cold rolled MP35N revealed a ring pattern with a single ring corresponding to hexagonal martensite. The intensity of the ring patterns would suggest a large volume fraction of hexagonal martensite but subsequent x-ray diffraction experiments were unable to detect its presence [9].

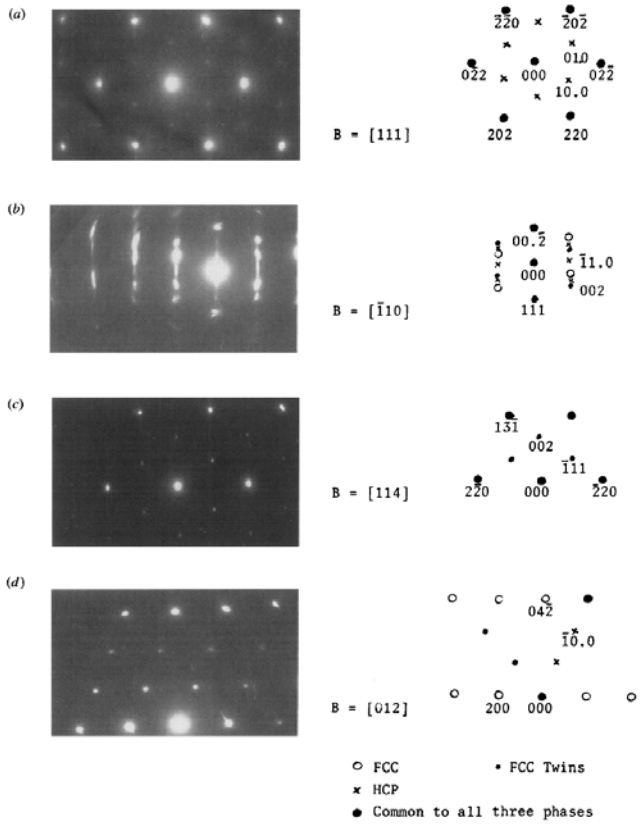

Figure 1.3 - Electron diffraction patterns of 48% cold worked MP35N showing the presence of diffraction spots from deformation twins, hcp platelets, or a mixture of all three [9]. Reprinted from Metallurgical Transactions, 23A, RP Singh, Strengthening in MULTIPHASE (MP35N) Alloy: Part I. Ambient Temperature Deformation and Recrystallization, Page 314, Copyright 1992, with permission from Springer.

1.3 THE SECONDARY HARDENING EFFECT IN MP35N

The strength of MP35N increases at a high rate following cold work as a result of deformation twinning. Aging heavily cold worked MP35N at elevated temperatures increases the strength further. The earliest discussion of the secondary hardening effect in MP35N was reported by Drapier et al. [7] and the mechanism was proposed to be segregation of Mo and Cr to the martensite phase. The preferential segregation of Mo

then results in the precipitation of Co_3Mo precipitates which strengthen the material upon aging [7]. Images of the proposed Co_3Mo precipitates were not reported. The next investigation related to the secondary hardening mechanism in MP35N was performed by Raghavan et al [8]. Analysis of the aged samples showed varying degrees of fine particles identified as hexagonal ε phase from the presence of a $(0\bar{1}10)_\varepsilon$ reflection. Figure 1.4 shows the dark field image and selected area diffraction pattern. The electron microscope work in this study [8] instead reported the ε phase to be fine precipitates in the austenite matrix and they were only present when the cold worked sample had been aged.

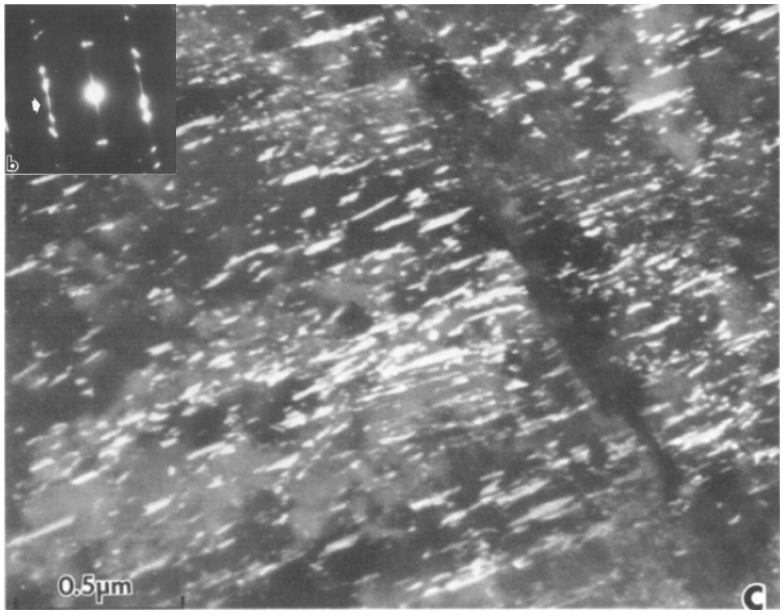

Figure 1.4 – Dark field image and corresponding SAD pattern of proposed ε precipitates [8]. Reprinted from Metallurgical Transactions A, 11A, M. Raghavan, BJ Berkowitz, and RD Kane, A Transmission Electron Microscopic Investigation of Phase Transformations in MP35N, Page 206, Copyright 1980, with permission from Springer.

The most thorough historical investigation into the mechanism of secondary hardening in MP35N was performed by Asgari et al [10]. In this body of work, commercially drawn rods between 48% and 53% cold work were annealed to obtain average grain sizes of 300 μm, 35 μm, and 1 μm. The effects of secondary hardening were studied using uniaxial compression tests to deform the materials to known true strain values followed by an aging cycle of 593°C for 4 hours. Following the aging process, the samples were further deformed in compression and the flow stress was measured. The increase in flow stress following aging, $\Delta\sigma$, was plotted against the flow stress prior to aging and was plotted for each grain size analyzed as shown in Figure 1.5. The authors observed overall that the secondary hardening was a function of the prior flow stress. In addition to this, they observed a phenomena the authors defined as strain softening which occurs when the prior flow stress was between 1600 MPa and 1700 MPa and the yield strength increase upon aging was over 200 MPa [10]. The mechanism of strain softening was determined to be a result of strain localization in shear bands. These observations showed secondary hardening was a function of the prior flow stress.

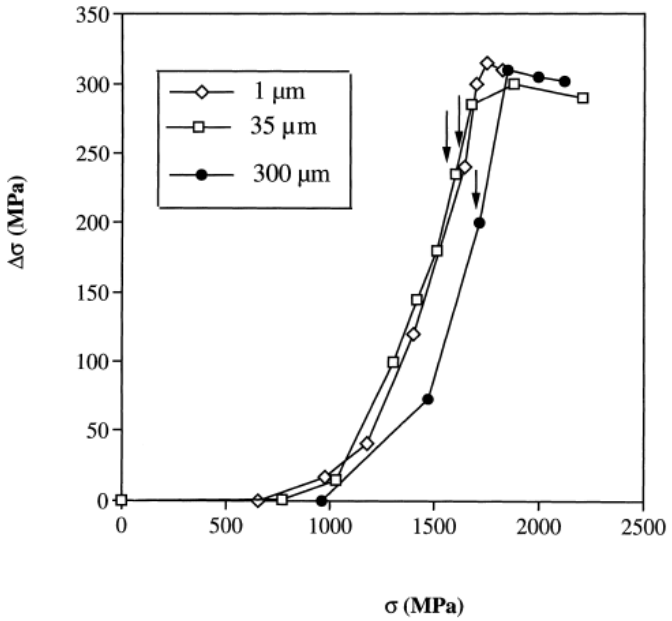

Figure 1.5 - Increase in yield strength plotted as a function of prior flow stress in MP35N with three separate grain sizes [10]. Reprinted from Acta Materialia, Vol 46, No.16, S. Asgari, E. El-Danaf, E. Shaji, SR Kalindindi, and RD Doherty, The Secondary Hardening Phenomenon In Strain-Hardened MP35N Alloy, Page 5798, Copyright 1998, with permission from Elsevier.

Transmission electron microscopy was performed on samples of MP35N with a grain size of 35 µm deformed to strains ranging from 0.09 (flow stress of 750 MPa) to 0.25 (flow stress of 1100 MPa). At strains of 0.09 and 0.15 without aging, the microstructure consisted of planar arrays of dislocations and stacking faults identified by their characteristic fringe patterns [10] as in Figure 1.6 below.

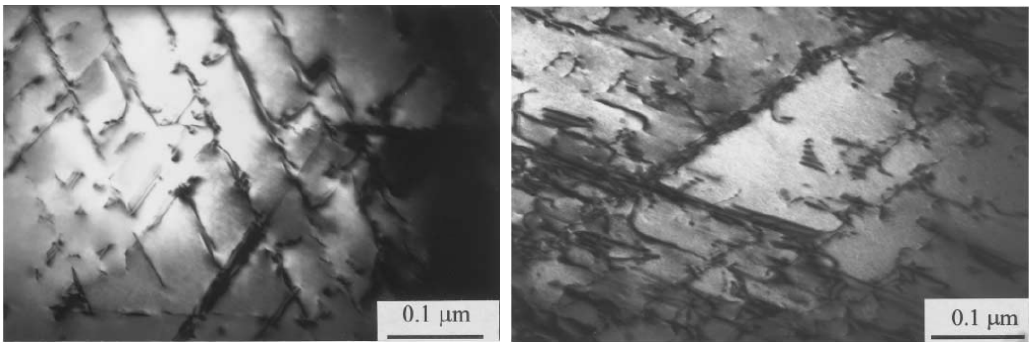

Figure 1.6 - Bright field TEM images of MP35N deformed to a strain of 0.09 (left) and 0.15 (Right) [10]. Reprinted from Acta Materialia, Vol 46, No.16, S. Asgari, E. El-Danaf, E. Shaji, SR Kalindindi, and RD Doherty, The Secondary Hardening Phenomenon In Strain-Hardened MP35N Alloy, Page 5799, Copyright 1998, with permission from Elsevier.

Transmission electron microscope investigations of MP35N samples deformed to 0.15 and 0.25 strain followed by aging at 593°C for 4 hours showed no signs of precipitation that could account for the increase in strength following aging. Instead stacking faults were identified by their characteristic fringe patterns [10]. The stacking faults observed in the sample deformed to 0.15 strain could not be correlated to any change in properties as no increase in flow stress was observed. The sample strained to 0.25 and aged was found to have an incremental flow stress increase of approximately 20 MPa. This increase in strength was attributed to an increase in stacking fault size and number of overlapping faults and twins (Figure 1.7). The increase in stacking fault size with additional deformation and aging was proposed to be a result of the Suzuki mechanism [11].

As previously mentioned, MP35N is a low stacking fault energy alloy in which perfect dislocations dissociate into partial dislocations. As partial dislocations glide on {111}

planes stacking faults are created by the leading partial while the perfect atomic arrangement is restored by the trailing partial. The faulted region between stacking faults in an FCC metal is a thin layer of HCP phase. As the cohesive energy in the hexagonal phase is different from the cubic phase, the concentration of solute atoms in the stacking fault would not be expected to be equal to that in the bulk material. This inhomogeneous distribution of solute atoms will then hinder dislocation motion similar to a Cottrell atmosphere. The mechanism of Suzuki segregation was first proposed by H. Suzuki [11, 12] and is based on the principle that the energy of an atom at a stacking fault may be different from its energy in the bulk lattice. This results in preferential segregation of energetically favorable solute atoms to the stacking fault. The driving force for this reaction is similar to adsorption of solute atoms to grain boundaries and can be described using the Gibbs adsorption isotherm [13],

$$\left(-\frac{\partial\gamma}{\delta\overline{G_2}}\right)_T = \Gamma_2 - \frac{x_2}{x_1}\Gamma_1 \quad (1)$$

x_1 and x_2 are the atomic fractions of solvent and solute in the bulk matrix respectively, $\overline{G_2}$ is the chemical potential of the solute atoms, γ is the stacking fault energy, and Γ_1 and Γ_2 are surface excess concentrations of solvent and solute at the fault. For dilute solutions where $\Gamma_2 > \left(\frac{x_2}{x_1}\right)\Gamma_1$ the Gibbs adsorption isotherm reduces to

$$\left(-\frac{\partial\gamma}{\delta\overline{G_2}}\right)_T = \Gamma_2 \quad (2)$$

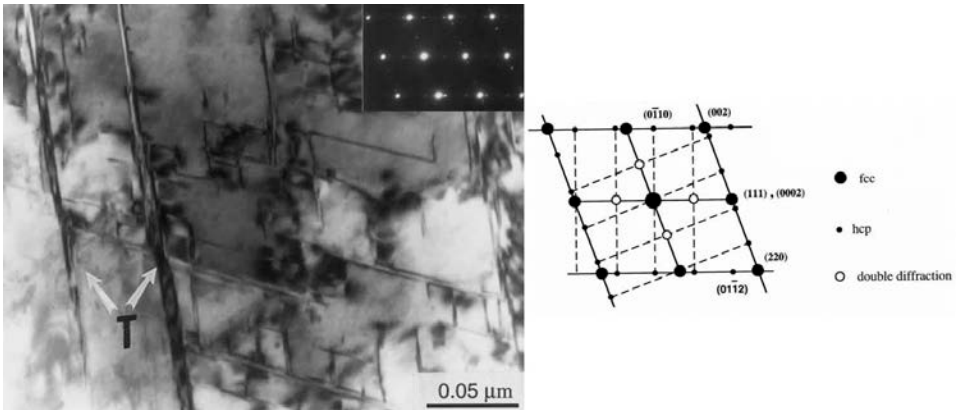

Figure 1.7 - Bright field transmission electron micrograph with inset selected area diffraction pattern (left) and indexed diffraction pattern (right) of cold worked and aged MP35N [10]. Reprinted from Acta Materialia, Vol 46, No.16, S. Asgari, E. El-Danaf, E. Shaji, SR Kalindindi, and RD Doherty, The Secondary Hardening Phenomenon In Strain-Hardened MP35N Alloy, Page 5803, Copyright 1998, with permission from Elsevier.

Prior to the work of Asgari et al. [10] few papers related to the processing-properties-performance-microstructure relationship of MP35N had been published. Ishmaku and Han [14] studied heavily cold rolled and aged MP35N sheet and plate and while plate-like features were observed, they were not identified as a specific phase, only as “platelets” [14]. More recent work published by Otomo et al. [15] reported the elastic modulus of MP35N slightly decreased following cold swaging but recovered upon annealing at high temperatures. This finding was attributed to dislocation locking resulting from the Suzuki mechanism and the preferred crystallographic orientation caused by cold rolling [15]. The most recent research involving the mechanism of secondary hardening in MP35N was performed by Cai et al. [16]. This thorough study utilized TEM and synchrotron x-ray diffraction studies to determine the mechanism of secondary hardening in heavily cold worked MP35N. The presence of a hexagonal

close packed phase was not identified in the TEM or synchrotron studies and the mechanism of age hardening was proposed to be the formation of nanotwins upon aging.

Active research has been underway to better the secondary hardening mechanism in MP35N from 1970 until the present day. While the proposed mechanisms of secondary hardening have been varied and controversial this body of work will take a different approach to understanding the phenomena of secondary hardening using analytical transmission electron microscopy to probe the local chemistry of the microstructure in a variety of material conditions.

2 EXPERIMENTAL PROCEDURE

2.1 SAMPLES

MP35N rod and wire samples were obtained from Accellent (Salem, PA) and Fort Wayne Metals (Fort Wayne, IN) with varying amounts of prior cold work. Table 1 below lists the materials used in this body of work. The chemistry of the alloys analyzed in this study is shown in Table 2 below.

Table 1 - Materials used in this study.

Sample	Form (diameter)	Prior Cold Work	Supplier
A	Wire (178 µm)	37%	Fort Wayne Metals
B	Wire (178 µm)	60%	Fort Wayne Metals
C	Wire (178 µm)	26%	Fort Wayne Metals
D	Rod (3 mm)	24%	Accellent
E	Rod (3 mm)	48%	Accellent
F	Rod (3 mm)	<5%	Accellent

Table 2 - Elemental composition of MP35N samples listed in Table 1. The values are in wt. %. The balance is Co. NM* - Not measured due to material availability.

Sample	Ni	Cr	Mo	Ti	C	S	P	B	Mn	Si	Fe
A	35.9	19.72	10.21	<0.005	0.0115	<0.0023	<0.005	0.016	0.020	0.075	0.080
B	35.88	19.57	10.14	0.018	0.0160	0.0025	<0.005	0.005	<0.005	0.076	0.083
C	33.72	20.18	9.17	<0.005	NM*	NM*	<0.005	0.006	0.020	0.075	0.027
D, E, and F	34.9	20.56	9.47	0.69	0.009	0.001	0.002	0.010	0.01	0.01	0.23

2.2 HEAT TREATMENT

The secondary hardening effect in MP35N is most pronounced in fine wires used in the medical device industry where short heat treatments during processing may have a significant effect on mechanical properties and performance of the final device. During the processing of MP35N from bare wire into a polymer insulated coil or cable, the material experiences numerous heating and cooling cycles. For example, Ethylene tetrafluoroethylene (ETFE) or Polytetrafluoroethylene (PTFE) is coated on the wires by stringing the MP35N wire through a polymer suspension followed by a sintering process at a temperature of approximately 400°C. In order to reach a desired insulation thickness, this process may need to be performed multiple times. Another high temperature process commonly used when manufacturing medical devices is known as a “thermal kill” process. In the thermal kill process MP35N wires are wound into wire rope or cable and subjected to a final stress relief temperature of 800°C to 900°C approximately 10 seconds. This process is required to keep the cable from unwinding as a result of residual stresses from the cable winding process.

The aging treatments on wires and rod used for all analyses in this paper with the exception of fatigue test samples were performed using a calibrated muffle furnace in an air atmosphere. The wire spool used for spin fatigue testing was heat treated in a tube furnace under a controlled atmosphere to achieve a bright, oxide free surface. An oxide

free surface reduces premature fatigue failures originating from crack formation on the thick thermal oxide. Samples of rodstock were cut into disks with a thickness of approximately 2 mm and placed on a commercial purity titanium pan. When the furnace was at temperature the samples were quickly placed in the furnace and the door was closed immediately in order to maintain the temperature. In most cases the temperature drop in the furnace was negligible or was small enough to allow the furnace to reach temperature again in approximately 10 seconds. Following the aging treatment the samples and pan were placed on a block of aluminum and allowed to cool in air. It was found the mechanical properties as measured in tension were statistically not affected by a thermal oxide or lack thereof.

2.3 MECHANICAL (TENSION) TESTING OF MP35N WIRE

Measuring the tensile stress-strain behavior of a material is one of the most common methods of characterizing its mechanical properties. The engineering stress, σ, of a material can be defined by the force, F, by the initial cross section of the sample, A_0.

$$\sigma = \frac{F}{A_0} \tag{3}$$

Similarly, the engineering strain, ε, is defined by the change in sample length, ΔL, divided by the original length, L_0.

$$\varepsilon = \frac{\Delta L}{L_0} \tag{4}$$

The elastic modulus, E, can then be calculated by measuring the slope of the stress-strain curve in the elastic region (prior to the onset of plastic deformation) and is defined as:

$$E = \frac{\sigma}{\varepsilon} \tag{5}$$

In this study the elastic modulus was measured between the first point on the stress-strain curve without residual slack from the sample settling in the jaws and the point

where the elastic modulus line deviates from linearity on the stress strain curve. Following final fracture, the samples were all analyzed for reduction in cross sectional area, the appropriate indicator of localized ductility. The reduction in area (RA) measurement was performed by carefully removing 1 cm of wire from the fractured end of the specimen with a wire cutter and placing the sample flat on an electron microscope stub with sticky carbon tape. The reduction in area measurement was then taken by measuring the nominal thickness of the wire, d_0, and the thickness at the minimum cross section in the necked region, d_n, near the fracture. The reduction in area was then calculated by:

$$RA\% = (1 - \frac{d_n}{d_0}) * 100 \quad (6)$$

The mechanical properties of individual MP35N wires heat treated at temperatures ranging from 300°C to 1000°C for times ranging from 30 seconds to 1 minute were measured. All wire samples were cut to 30.5 cm (12 inch) lengths and tested using an MTS QTest 5 load frame with a 250 N load cell. The strain and elastic modulus was measured using an MTS LX500 laser extensometer. All samples were tested with a 25.4 cm (10 inch) gage length and a crosshead speed of 0.02 cm*sec^{-1} (0.50 in*min^{-1}).

2.4 SAMPLE PREPARATION FOR ELECTRON BACKSCATTER DIFFRACTION

The quality of electron backscatter diffraction analyses is very sensitive to sample preparation techniques and the sample surface. Improper sample preparation, surface smearing, preparation induced surface strain, and scratches can degrade the quality of EBSD data sets significantly [17]. For each cold work and heat treatment condition, 10 wires were mounted in the transverse direction by using thin strips of masking tape to fix the wires on a larger MP35N rod that was free standing. This process allowed all wires to be mounted, prepared, and analyzed in the transverse (wire drawing) direction. In this

study, samples for electron backscatter diffraction analysis were mechanically polished using a method to minimize residual damage or surface strains from the preparation process. Several MP35N wires from each condition were mounted in the transverse direction in ProbeMet conductive mounting compound and prepared using a Buehler EcoMet/AutoMet 250 using the following procedure:

I. Grind the samples using 320 grit pressure sensitive adhesive (PSA) backed paper until plane and scratch pattern is uniform.
II. Polish using 15 μm polycrystalline diamond suspension and a Buehler TexMet 1000 pad for 5 minutes.
III. Polish using 9 μm polycrystalline diamond suspension and a Buehler UltraPol pad for 7 minutes.
IV. Polish using 6 μm polycrystalline diamond suspension and a Buehler TexMet 1000 pad for 5 minutes.
V. Polish using 3 μm polycrystalline diamond suspension and a Buehler TriDent pad for 5 minutes.
VI. Polish using 1 μm polycrystalline diamond suspension and a Buehler TriDent pad for 5 minutes.
VII. Polish using 0.25 μm polycrystalline diamond suspension and a low napped Buehler MasterTex pad for 3 minutes.
VIII. Final polish using 0.02 μm Buehler MasterMet 2 non-crystallizing colloidal silica and a medium napped Buehler MicroCloth pad for 7 minutes.
IX. A four hour vibratory polish on each sample using Buehler MasterMet 1 colloidal silica, a Buehler MasterTex polishing pad, and two vibratory polisher weights was

performed to relieve any residual surface strains introduced during the preparation process [17].

The 320 grit grinding step was performed using 6 lbf per sample, a platen speed of 250 RPM, a polishing head speed of 60 RPM, and contra rotation until the samples were plane. The diamond and colloidal silica polishing steps were performed using 6 lbf per sample, a platen speed of 160 RPM, and a polishing head speed of 60 RPM.

2.5 ROTARY BEAM FATIGUE TESTING

Rotary beam fatigue testing is a commonly used method to determine fatigue behavior in fine wire sample under alternation tension-compression conditions with an R value of -1. The technique is performed by fixing one end of a wire in a chuck while the other end is free to rotate in a bushing. The chuck rotates at 60 Hz and the number of rotations is measured by a calibrated counter. All testing was performed on Valley Instruments Model 100 wire fatigue testers. The digital readout that displays the number of cycles was calibrated before use. All wires were carefully straightened in the rotating chuck by hand prior to beginning each test. After the beginning of a test, if a wire appeared to excessively wobble, the test was stopped and the wire was removed and replaced. The elastic modulus for each wire heat treatment condition was measured using an MTS LX500 laser extensometer with a sample size of n=3 and averaged. The equations and values required for rotary beam fatigue testing can be found in Table 3. The wire fatigue test set up along with the important dimensions, including center distance between wires (C), wire bend radius (R), height (h), and length of wire tested (L), can be found in Figure 2.2 below.

Table 3 - Spin fatigue test parameters and equations

Parameter	Equation
Center Distance (C)	$\frac{1.198 * E * d}{S}$
Minimum Radius (R)	$0.417 * C$
Height (h)	$0.835 * C$
Test Length (L)	$2.19 * C$

Where E, d, and S are the elastic modulus (psi), wire diameter (inches), and desired test stress (psi), respectively. Following each fracture event the lengths of the wire halves were measured in order to determine a corrected stress in the event failure did not occur at the bend apex. In this study, run out was defined as 10,000,000 cycles without a fracture.

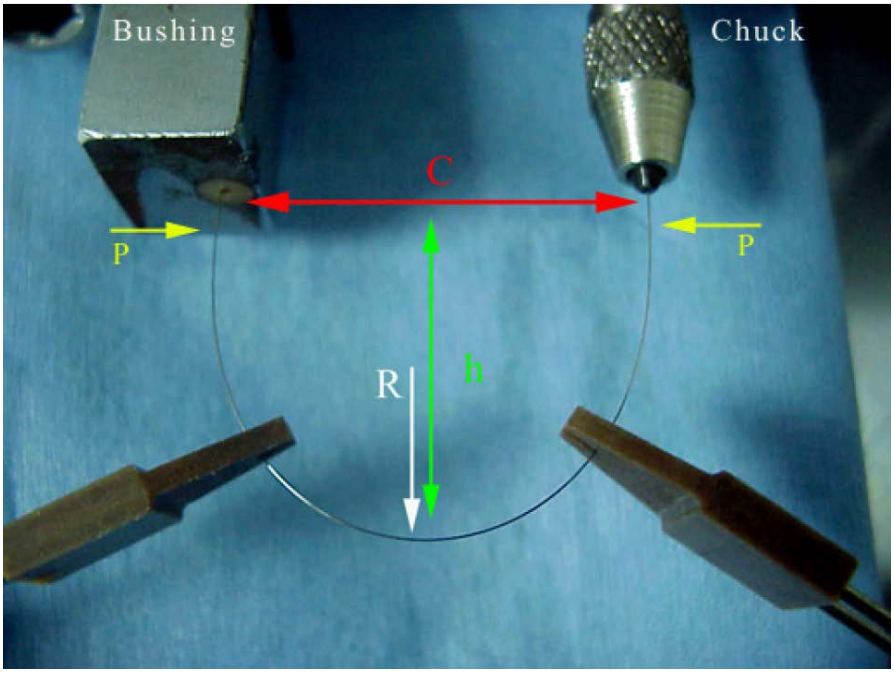

Figure 2.1 - Rotary beam fatigue test geometry and parameters.

2.6 ELECTRON BACKSCATTER DIFFRACTION (EBSD)

Electron backscatter diffraction is a powerful tool for meso-scale microstructural analysis of metals, alloys, and ceramic materials. A careful EBSD experiment can yield information about a materials crystallographic orientation, grain size, grain boundary character, and phases present. Figure 2.3 shows the inside of a scanning electron microscope with an EBSD detector and sample tilted to the optimal angle for data collection.

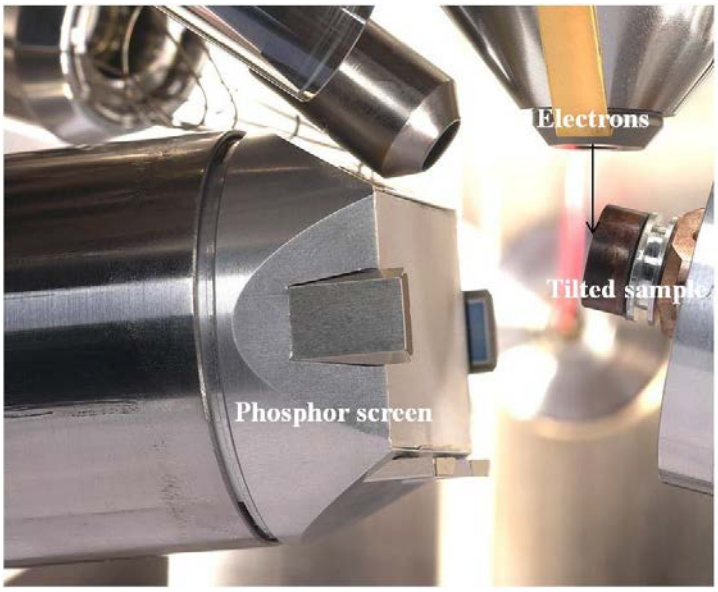

Figure 2.2 - Image of the inside of an SEM chamber showing the relationship between a sample, phosphor screen, and electron beam [18].

Electron backscatter diffraction experiments were performed on a Zeiss Ultra Plus field emission scanning electron microscope (FESEM) with an EDAX EBSD detector attachment. EBSD was performed on three separate wire sections from each heat treatment and cold work condition to ensure a statistical sampling of each condition was obtained. Each scan on 37% cold worked wire specimen was taken on an approximately 100 μm^2 area at a magnification of 2,000X and step size of 0.15 μm.

Samples of 60% cold worked wire were scanned over an area of approximately 40 μm^2 at a magnification of 5,000X and a step size of 0.1 µm. A smaller area was scanned for the 60% cold worked material as the grains were smaller and the larger amounts of residual strain in the wire yielded large areas of low image quality and confidence index at lower magnifications. Scanning a 40 μm^2 area allowed a representative area with a reasonable image quality to be quantitatively analyzed. The length calibrations in both the EDAX TSL OIM and Zeiss Smart SEM software was verified using the known diameter of the cross sectioned MP35N wires.

2.7 TRANSMISSION ELECTRON MICROSCOPY SAMPLE PREPARATION

Electron transparent samples for TEM analysis were prepared based on the bulk sample geometry. Large MP35N rodstock samples were first machined down to 2.9 mm diameter. Following the machining process, disks approximately 200 µm of material were cut from the rod using an IsoMet Low Speed precision saw using a 0.4 mm diamond blade and de-ionized water as a lubricant. The disks were further thinned by grinding using 600 and 1200 grit abrasive papers to a thickness ranging from 40 µm to 80 µm. All samples were electro polished using a Fischione twin jet electro polisher operating at 10 V with a solution of H_2SO_4, H_3PO_4, and methanol at 0°C to 25°C.

Fine wire TEM samples were prepared using both FEI Quanta and FEI Versa 3D dual beam focused ion beam (FIB) milling and in-situ lift out using an Omniprobe micro-manipulator. Images of a TEM lamella during lift out and following final thinning can be seen in Figure 2.4.

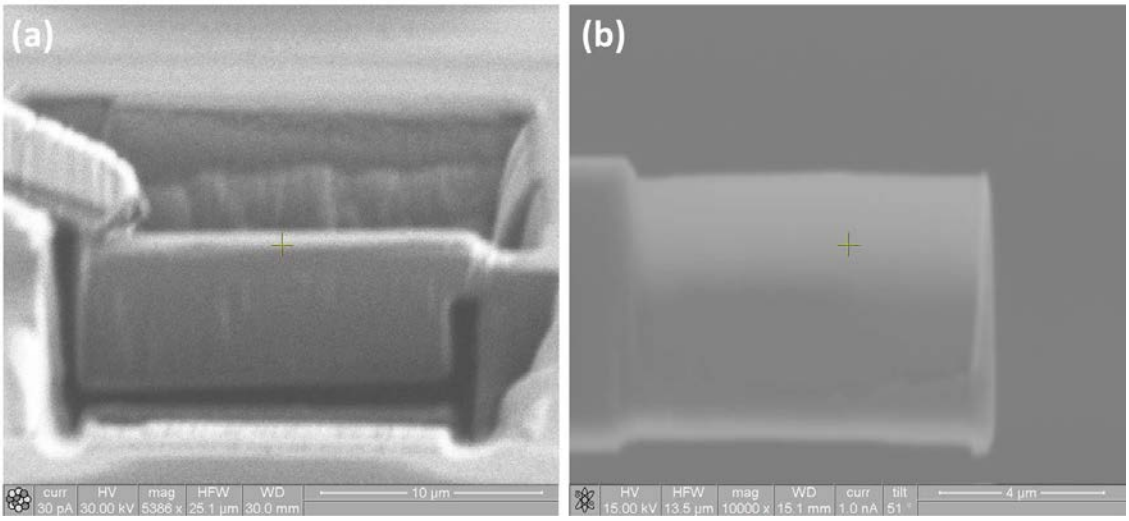

Figure 2.3 - Secondary electron micrographs showing (a) Lamella during in-situ lift out and (b) following final ion polishing steps.

2.8 CONVENTIONAL TRANSMISSION ELECTRON MICROSCOPY (CTEM)

Conventional transmission electron microscopy was performed on an FEI Technai G^2 T12 operating at 120 kV and an FEI Tecnai G^2 F30 field emission gun (FEG) TEM operating at 300 kV.

2.9 ANALYTICAL SCANNING TRANSMISSION ELECTRON MICROSCOPY (STEM)

Analytical scanning transmission electron microscopy was performed using an FEI Tecnai G^2 F30 FEGTEM operating at 300 kV using an EDAX EDS detector and Gatan electron energy loss spectrometer.

3 RESULTS

3.1 MICROHARDNESS OF MP35N RODSTOCK AS A FUNCTION OF HEAT TREATMENT TEMPERATURE

Microhardness testing of fully annealed MP35N 3 mm rodstock following a variety of aging treatments showed no statistically significant effect on the material hardness. This observation agrees with experiments performed by Drapier et al.[7]. Hardness testing of MP35N rodstock with 25% prior cold work aged for 1800 seconds (30 minutes) at temperatures ranging from 300°C to 1000°C showed a small increase in microhardness peaking at 600°C and gradually falling at higher aging temperatures. The final rodstock sample with 48% cold work showed a gradual increase in microhardness with respect to aging temperature, peaking at 600°C followed by a rapid decrease in hardness. The calculated yield stress converted from microhardness using the accepted relationship of H/3 is plotted versus aging temperature for all three processing histories in Figure 3.1. Aged MP35N with 48% cold work was found to harden to a higher degree than the samples with lower amounts of cold work prior to thermal treatments.

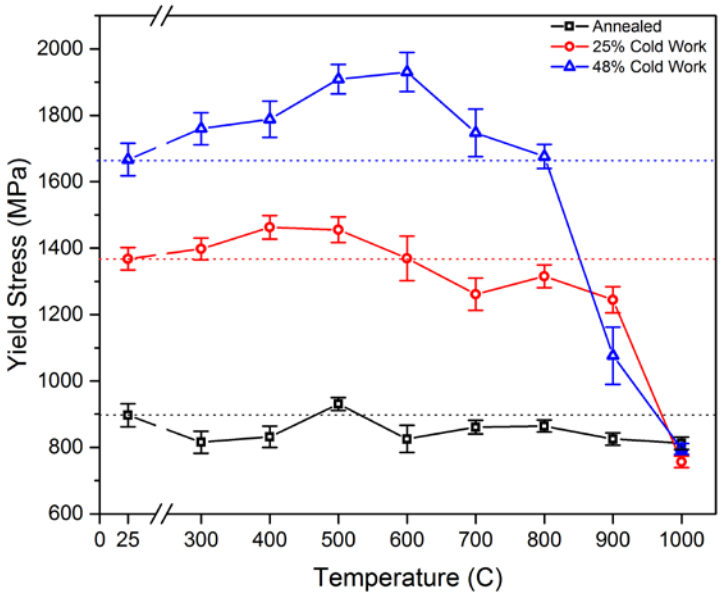

Figure 3.1 - Interval plot showing effect of 30 minute aging treatment on MP35N rodstock that has been fully annealed, cold worked 25% and cold worked 48%. Error bars signify a 95% confidence interval from the mean.

3.2 MP35N WIRE: MECHANICAL PROPERTIES AS A FUNCTION OF AGING TEMPERATURE

Compared to the 3 mm rodstock, results from more highly cold worked wire samples will be presented and discussed next. Figure 3.2 and Figure 3.3 below show the ultimate tensile strength and offset yield stress as a function of a 60 second aging treatment on 178 μm (0.007 inch) diameter MP35N wire. Two lots of wire, each with a different amount of cold work were tested to investigate the sensitivity to secondary hardening on the initial dislocation density in the wire. For this work, wires with 37% and 60% cold work were analyzed. The results show both wires have a gradual increase in strength that reaches a peak value at 700°C and gradually decreases as the temperature for the onset of recrystallization and recovery is reached. The degree of strengthening was found to be proportional to the dislocation density (amount of prior cold work). As the aging temperature reached approximately 800°C the ultimate tensile strength and offset

yield stress begin to rapidly decrease as seen in Figure 3.2 and 3.3. The wire with 60% prior cold work began to recover much more rapidly as the driving force for recrystallization is larger due to a higher initial dislocation density. The increased spread in ultimate tensile strength and 0.2% offset yield strength values in the 60% cold worked wire after a thermal treatment at 900°C is a result of partial recrystallization in the wires, as was confirmed using EBSD.

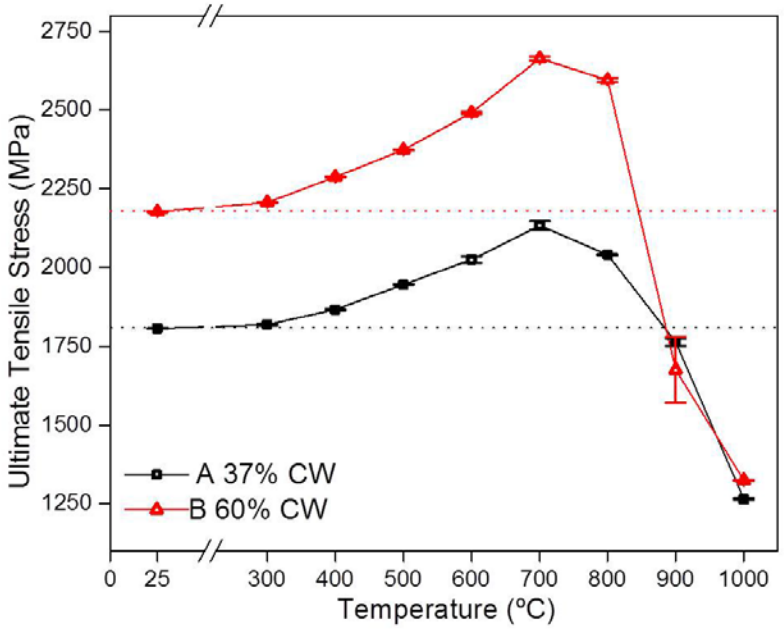

Figure 3.2 - Ultimate tensile stress as a function of aging temperature and prior cold work in wire Samples A and B. The samples were aged for 60 seconds. The error bars correspond to a 95% confidence interval.

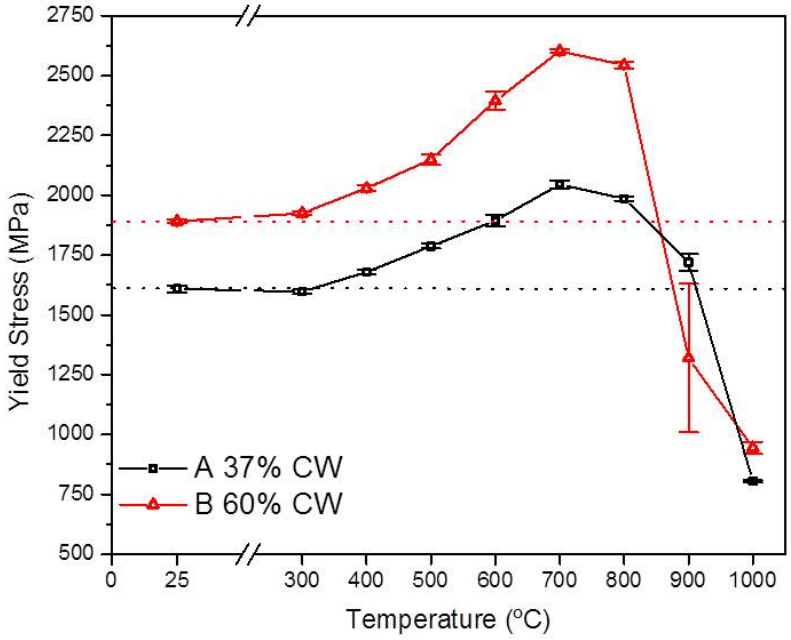

Figure 3.3 - 0.2% offset yield stress as a function of aging temperature and prior cold work in wire Samples A and B. The samples were aged for 60 seconds. The error bars correspond to a 95% confidence interval [19]. Reprinted with permission from Elsevier.

The ultimate tensile and 0.2% offset yield stresses increased, peaked at an aging temperature of 700°C, and started to decrease at the onset of recovery and recrystallization. The strain at fracture began to decrease continuously until the onset of recrystallization. The observation of decreases in the ultimate tensile and yield stresses in single phase metals and alloys is usually accompanied by an increase in ultimate elongation. The MP35N wires analyzed showed a decrease in break elongation as the thermal treatment temperature increased, even after a decrease in strength. The wire heat treated at 1000°C was fully recrystallized and found to have break strains on the order of 40% and was excluded from Figure 3.4 as to not mask the trend of decreasing break elongation prior to recrystallization.

.

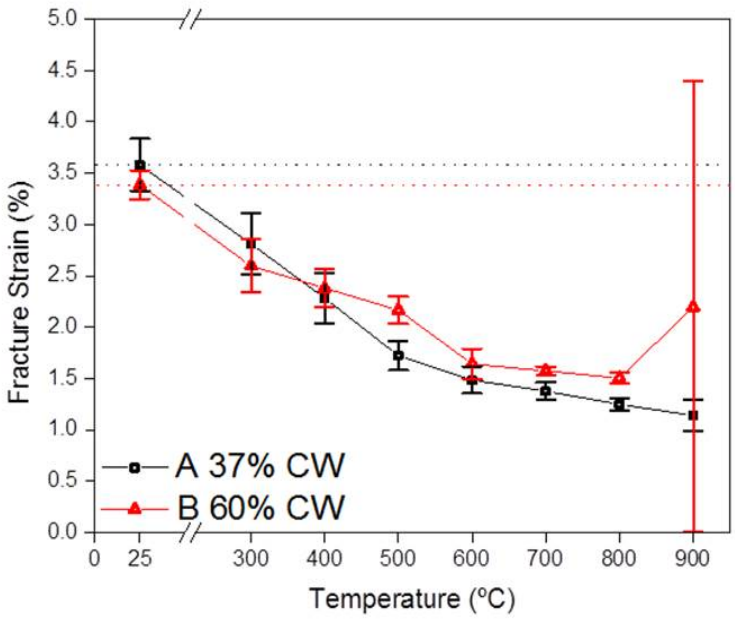

Figure 3.4 – Strain from elongation at fracture as a function of aging temperature and prior cold work in wire Samples A and B. The samples were aged for 60 seconds. The error bars correspond to a 95% confidence interval [19]. Reprinted with permission from Elsevier.

The decrease in ultimate elongation as a function of heat treatment temperature observed during the uniaxial tension testing was confirmed by measuring the RA of each fractured wire using SEM since this is a more appropriate measure of localized ductility. The fractures all showed signs of localized necking regardless of heat treatment condition except for one condition of 60% cold work. An interval plot showing the trend of decreasing RA values as the thermal treatment temperature increases for 37% cold worked MP35N wire can be found in Figure 3.5 below. Representative images of fractured wire samples showing the presence of microvoid coalescence on the fracture surface and large amounts of localized necking can be found in Figure 3.6.

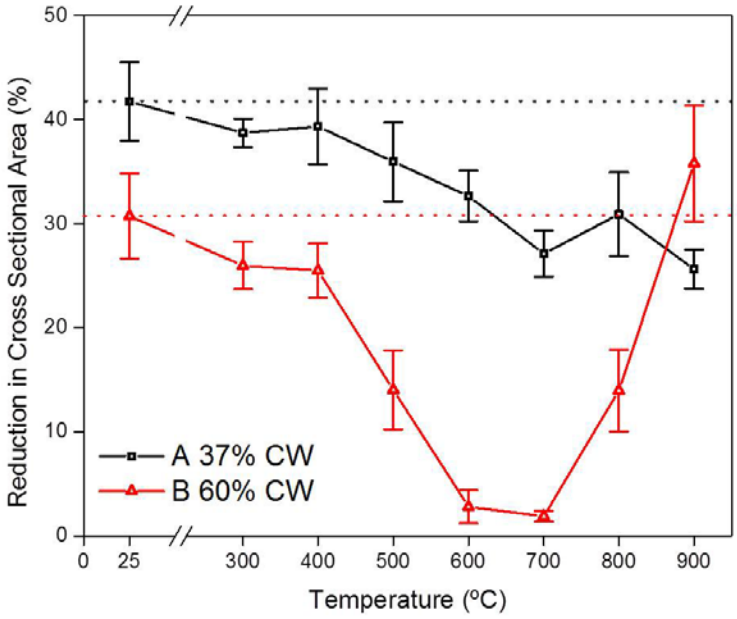

Figure 3.5 - RA measurements of Samples A and B as a function of aging temperature. The samples were aged for 60 seconds. The error bars correspond to a 95% confidence level [19]. Reprinted with permission from Elsevier.

MP35N wire with 60% prior cold work showed behavior slightly different than material with less cold work as shown in Figure 3.7. As expected the ductility of the 60% cold work as drawn material was much lower than wire with 37% cold work. The ductility decreased up to an aging temperature of 700°C, with the reduction in area correspondingly approaching zero. The decreasing ductility was determined to be caused by a localized shear instability as seen in Figure 3.7 (c). The strong <111> texture of the wire in the drawing direction and approximately 35 degree angle of the fracture surface makes it clear the fracture occurred on [110] planes as would be expected for a single crystal or highly textured FCC metal. This observation was consistent with historical investigations of high strength silver core MP35N wires that had experienced a brief aging treatment at high temperatures [20]. As the aging temperature increased to 800°C, a small increase in ductility was measured. At 900°C, the reduction

in area was found to be greater than the as drawn wire. This result was due to the partially recrystallized microstructure discussed further in section 3.4.

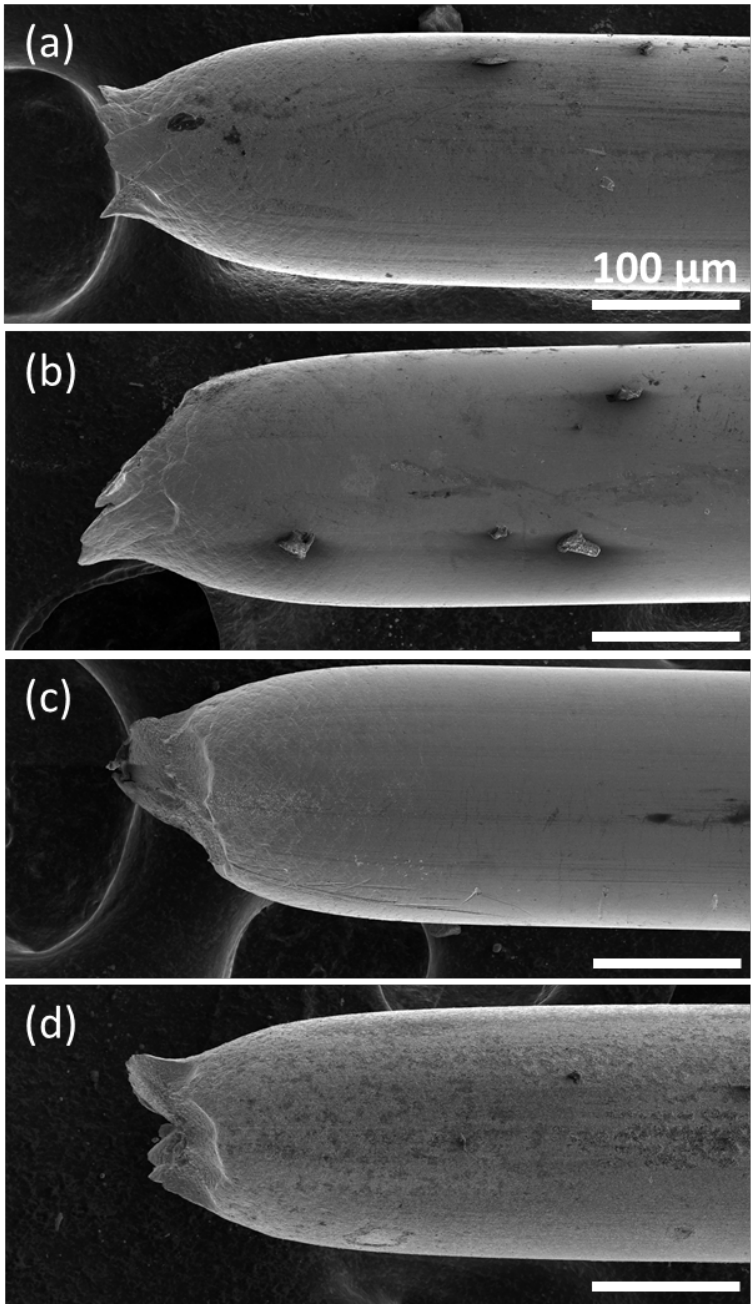

Figure 3.6 - SEM images of fractured MP35N wires from Sample A (37% prior cold work) following various thermal treatments: (a) as drawn (b) 500°C for 60 seconds (c) 700°C for 60 seconds (d) 900°C for 60 seconds [19]. Reprinted with permission from Elsevier.

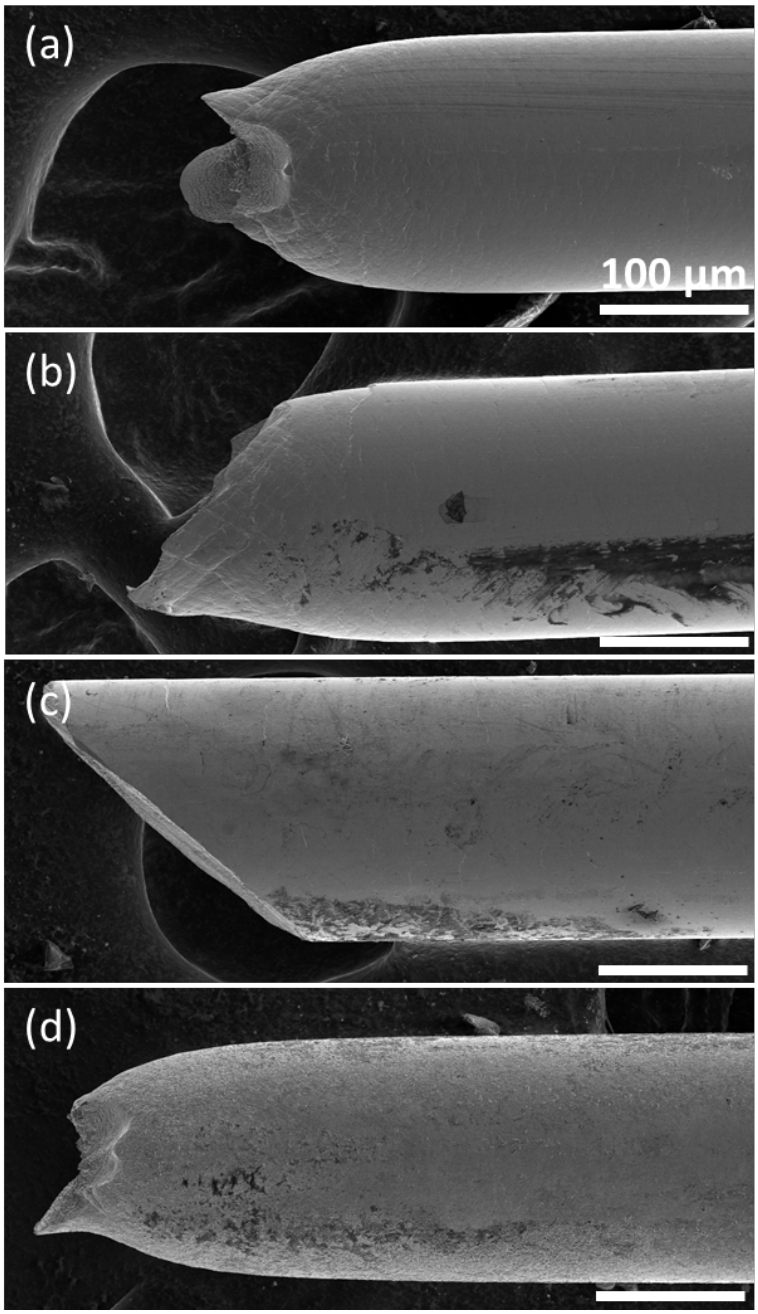

Figure 3.7 - SEM images of fractured MP35N wires from Sample B (60% prior cold work) following various thermal treatments (a) as drawn (b) 500°C for 60 seconds (c) 700°C for 60 seconds (d) 900°C for 60 seconds [19]. Reprinted with permission from Elsevier.

All wires were tested using a laser extensometer to accurately measure displacement and thereby strain of the wire within the gage length. This further enabled accurate determination of elastic modulus for the fine wires being tested. The measured elastic modulus was lower than typical reported values of MP35N [14, 15] for both 37% and 60% cold worked wire in the as drawn condition. This is likely an effect of the strong <111> crystallographic texture common to heavily cold worked MP35N wires and FCC metals in general [21]. Following a brief aging treatment at 300°C, the elastic modulus increased a statistically significant amount in both prior cold work wire conditions. Increasing the temperature further caused the elastic modulus to increase until the material was fully annealed and the elastic modulus approached the commonly reported values [14, 15] nearing 235 GPa. The line plot showing elastic modulus measured as a function of aging temperature for both Samples A and B (37% and 60% cold work respectively) can be found in Figure 3.8.

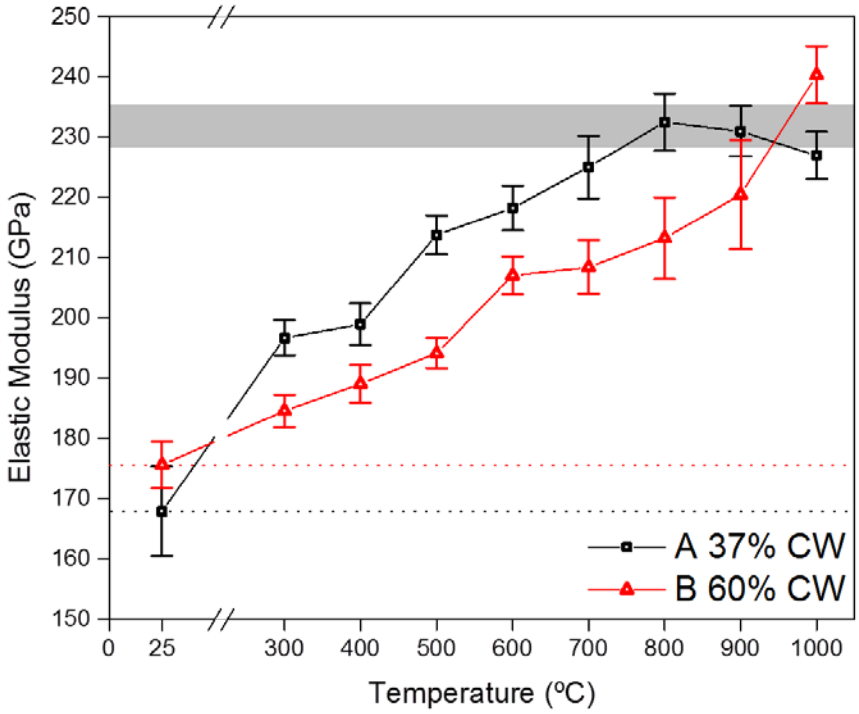

Figure 3.8 - Elastic modulus of MP35N wires (Samples A and B) measured as a function of aging temperature. The shaded gray region indicates the range of reported elastic modulus values for fully annealed MP35N sample [14, 15]. The error bars correspond to a 95% confidence level [19]. Reprinted with permission from Elsevier.

3.3 ROTARY BEAM FATIGUE TESTING

Rotary beam fatigue testing was performed on MP35N wire having 46% cold work. Heat treatments were performed on the wire at Fort Wayne Metals in a tube furnace under a reducing atmosphere. Initial wires aged using an air furnace resulted in a thin oxide that acted as a site for crack initiation under fatigue loading, which resulted in an artificially low number of cycles to failure. The elastic properties of each wire were measured by tension testing to ensure the correct Young's modulus was used to calculate the stresses for each wire condition. The average elastic properties measured and used for each heat treatment condition and fatigue test can be found in Table 4 below. The

microstructures of each wire condition were also analyzed to ensure that any changes in elastic properties or fatigue performance were not related to grain size or crystallographic texture. The electron backscatter diffraction orientation image maps and corresponding pole figures seen in Figure 3.9 show a consistent grain size and texture for each condition of wire fatigue tested.

Rotary beam fatigue testing was performed on each of the four wire conditions (as drawn, aged at 500°C for 1 minute, aged at 700°C for 1 minute, and aged at 900°C for 1 minute) at a variety of stress levels until run out, here defined to be 10,000,000 cycles, was reached. A stress value for run out was determined for all wire conditions, excluding samples aged at 500°C due to an issue of shortage of wire. For wire in the as drawn condition run out was found to be slightly below 550 MPa. Wire aged at 700°C for 1 minute achieved run out at a stress of 650 MPa. Lastly, wire aged at 900°C for 1 minute reached run out at a stress of approximately 690 MPa. The S-N curves for the rotary beam fatigue testing can be found in Figure 3.10.

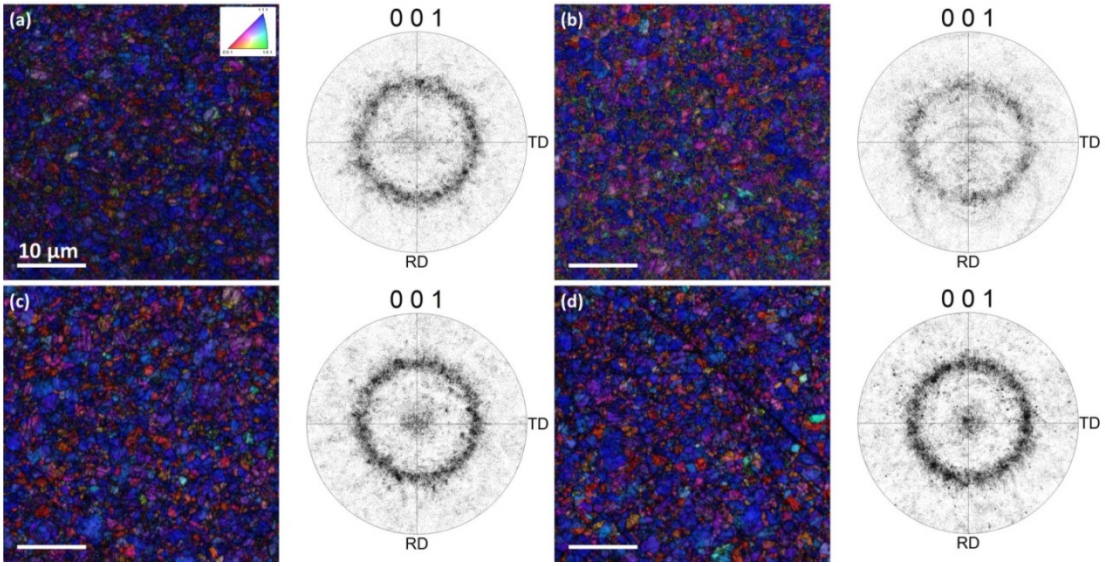

Figure 3.9 - Electron backscatter diffraction orientation image maps with image quality maps overlaid (OIM+IQ) and their corresponding pole figures for (a) as drawn MP35N wire with 25% cold work (b) 25% cold worked MP35N aged at 500°C for 1 minute (c) 25% cold worked MP35N aged at 700°C for 1 minute (d) 25% cold worked MP35N aged at 900°C for 1 minute

Table 4 - Experimentally measured elastic properties used for inputs to rotary beam fatigue testing.

Condition	**Average Measured Elastic Modulus (GPa)**	**Average Yield Stress (MPa)**	**Average Strain at Fracture (%)**
25% Cold Work As Drawn	177	1545	5.4
25% Cold Work, 500°C/60 second Aging	222	1764	1.7
25% Cold Work, 700°C/60 second Aging	234	1934	1.7
25% Cold Work, 900°C/60 second Aging	245	1488	12.6

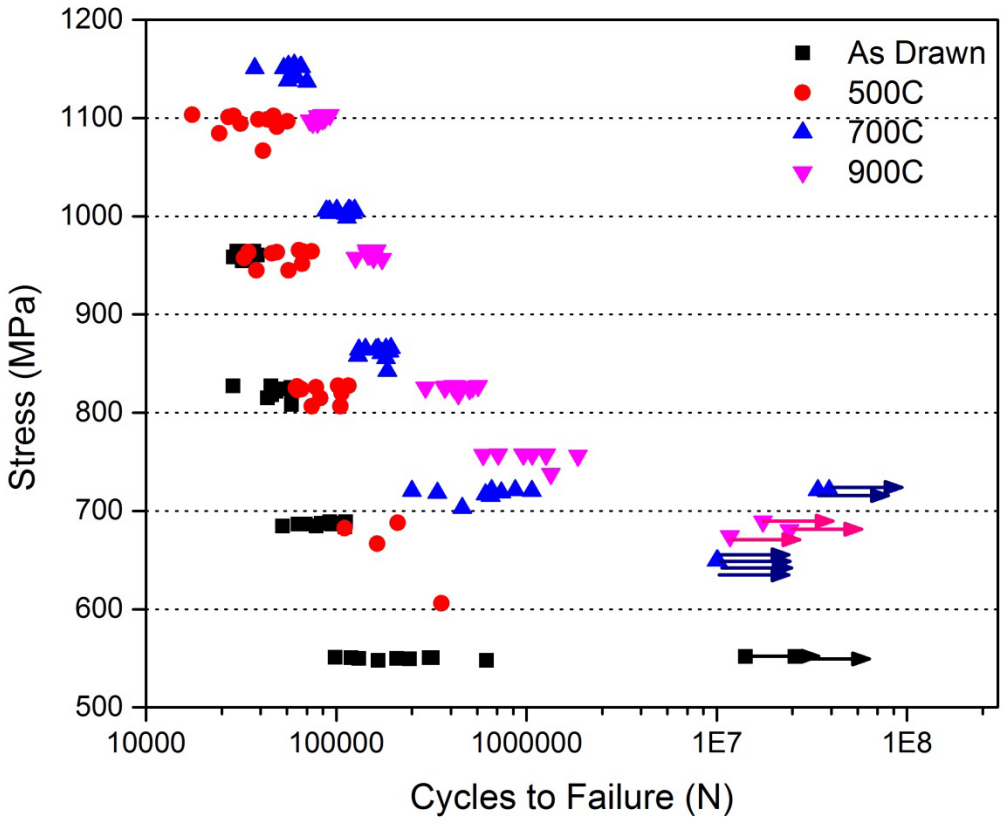

Figure 3.10 - Stress-cycles to failure (S-N) curves for MP35N wires with different aging treatments tested using rotary beam fatigue.

3.4 ELECTRON BACKSCATTER DIFFRACTION (EBSD)

Electron backscatter diffraction was used to obtain microstructural information from MP35N rod (3 mm) and wire (178 μm) that would be difficult or impossible to obtain using traditional metallographic techniques. The high dislocation density, small grain size, and small diameter of many of the samples would complicate chemical etching and possibly introduce artifacts such as pitting. Many quantitative analyses of microstructure can be performed in parallel via EBSD that can then be correlated with the measured mechanical properties of MP35N in the highly cold-worked and textured condition.

3.4.1 *MP35N RODSTOCK (3 MM DIAMETER)*

Orientation imaging microscopy was performed on 3 mm diameter MP35N rodstock in three cold work conditions; fully annealed, 25% cold work, and 48% cold work. The annealed sample was found to have a fully recrystallized microstructure with no appreciable crystallographic texture, large numbers of annealing twins, high angle grain boundaries, and an average grain size of 40 μm. MP35N rod with 25% cold work was shown to have a slightly textured microstructure coupled with orientation gradients within individual grains. Only a small number of deformation twins could be resolved by EBSD when investigating this material condition. Lastly, rodstock with 48% cold work was found to have a highly textured <111> orientation in the drawing direction. MP35N with 48% cold work was also found to have lower amounts of orientation gradients within individual grains. The concentration gradients were replaced by a large area fraction of deformation twins. Figure 3.11 shows the orientation map and pole figures for large grained MP35N in the fully annealed, 25% cold worked, and 48% cold worked condition.

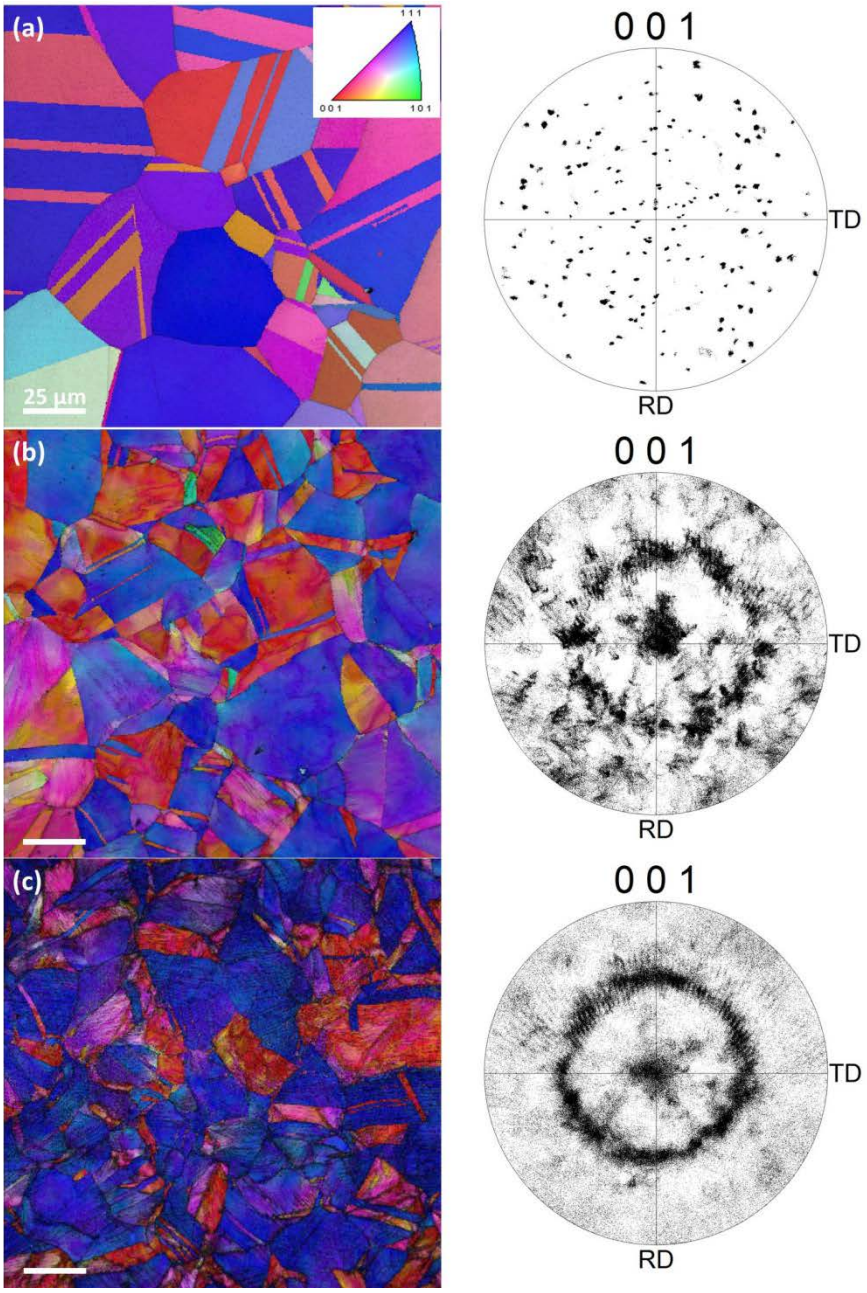

Figure 3.11 - Orientation image map and overlaid image quality map (OIM+IQ) pole figures showing (a) the random crystallographic orientation of fully annealed MP35N rod stock (<5% cold work) (b) slight texturing and orientation gradients within individual grains in 25% cold worked MP35N rod stock and (c) heavily <111> oriented MP35N with a large number of deformation twins following 48% cold work.

3.4.2 *MP35N WIRE (178 μM DIAMETER)*

EBSD analyses of wire samples were performed on sectioned and mechanically polished components mounted in the transverse direction. Multiple wires from each heat treatment condition were mounted together to ensure a representative sample size could be obtained. Three EBSD scans were performed on random wires in the mount to obtain a statistical sampling of texture, grain size, and area fraction of texture components for each condition. MP35N wire with 37% cold work was found to have a preferred <111> crystallographic orientation that was not altered appreciably during the thermal treatments. The microstructure consisted of fine grains with an average grain size ranging from 2 μm to 5 μm and annealing twins which were introduced from thermal treatments performed at intermediate steps during the wire drawing process. The crystallographic orientation of 60% cold worked MP35N wires was slightly different from wire with a lower amount of cold work. The orientation maps and pole figures showed a stronger <111> orientation but also a noticeable <100> texture component that was much less prominent in the 37% cold worked wires. Figure 3.12 below show representative orientation image maps overlaid on image quality maps (OIM+IQ) for six aging conditions in 37% cold worked MP35N wire following a one minute thermal treatment. The orientation maps and pole figures remained constant through each aging cycle up to 1000°C where full recrystallization occurred. Figure 3.13 shows the orientation map – image quality map overlay for 60% cold worked MP35N wire. The strong <111> and <100> texture remains constant until the aging temperature reached 900°C where strain-free recrystallized grains could be observed. The onset of recrystallization at temperatures below 1000°C can be rationalized by the high amounts of plastic strain in the 60% cold worked material providing the needed driving force. The

large plastic strain can be qualitatively visualized in Figure 3.12 and Figure 3.13 where the orientation map-image quality maps are overlaid. The darker color in the maps of 60% cold worked material signifies a lower image quality and therefore higher plastic strain in the material [22].

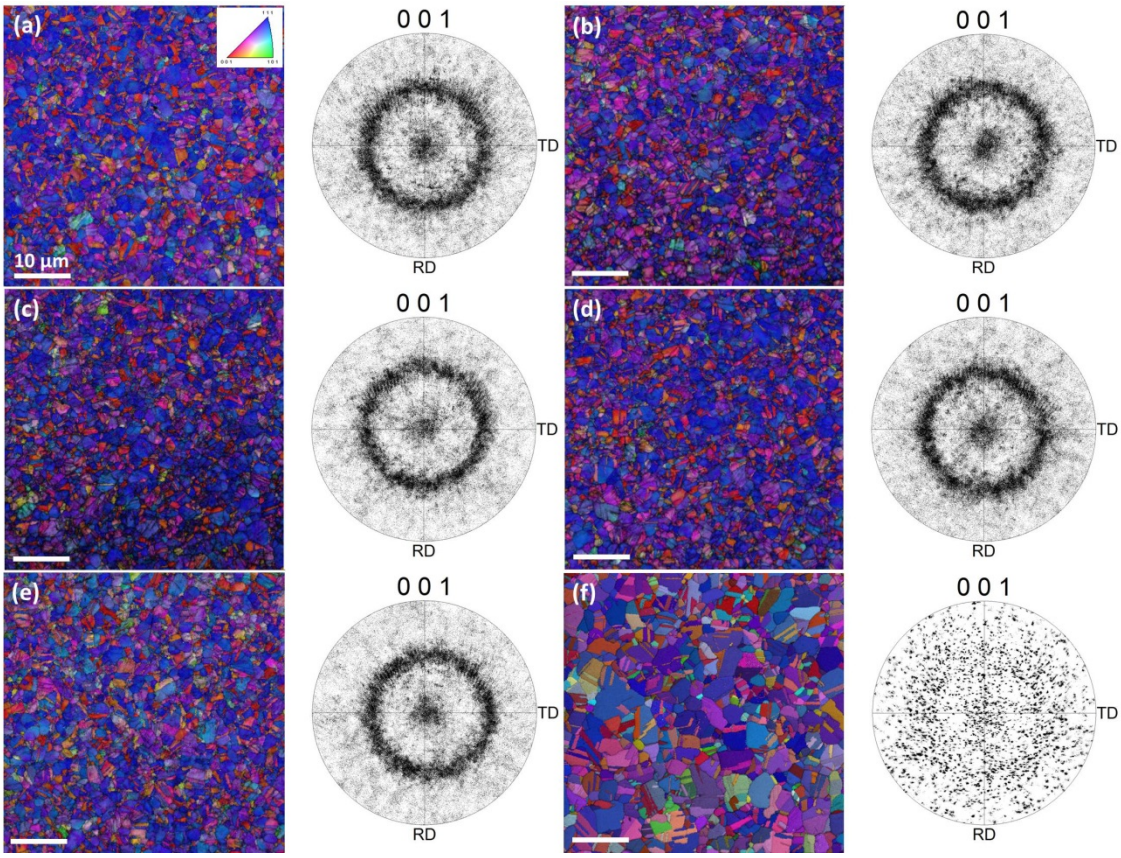

Figure 3.12 – Orientation image map with overlaid image quality map (OIM+IQ) and corresponding pole figure showing the strong <111> crystallographic orientation of 37% cold worked MP35N wire in the (a) as drawn condition (b) aged at 300°C for 1 minute (c) aged at 500°C for 1 minute (d) 700°C for 1 minute (e) 900°C for 1 minute and (f) 1000°C for 1 minute.

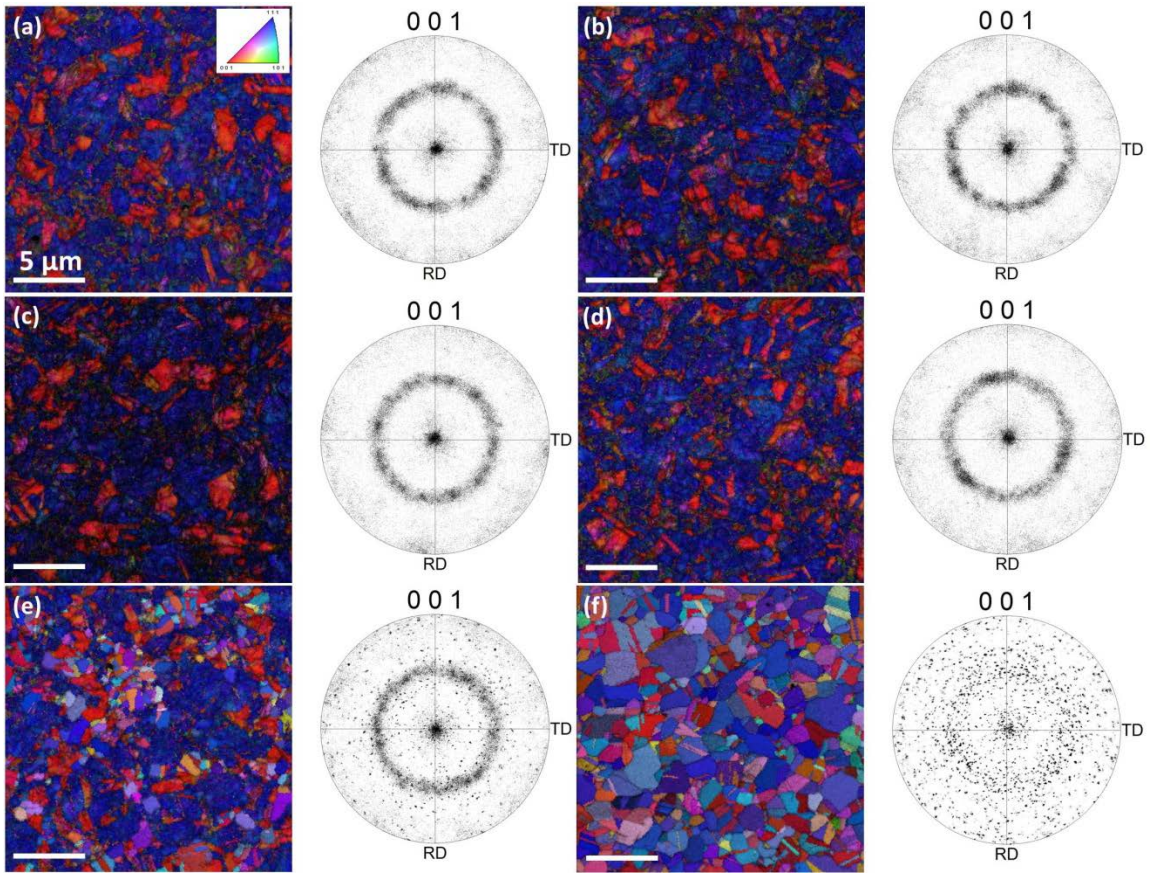

Figure 3.13 – Orientation image map with overlaid image quality map (OIM+IQ) and corresponding pole figure showing the strong <111> crystallographic orientation of 60% cold worked MP35N wire in the (a) as drawn condition (b) aged at 300°C for 1 minute (c) aged at 500°C for 1 minute (d) 700°C for 1 minute (e) 900°C for 1 minute and (f) 1000°C for 1 minute.

Three grain size distributions were collected for each thermal treatment and wire condition. The highest number fraction grain size in all the distributions was in the range of 2 μm to 5 μm. The number average grain size only began to increase at the onset of recrystallization (temperatures above 900°C). Figure 3.14 below shows an interval plot of the average grain size in the 37% and 60% cold worked MP35N wire as a function of heat treatment temperature. The results show short heat treatments below 1000°C do not have a statistically significant effect on the average grain size on the wires analyzed in this present study. The larger spread in average grain sizes observed for the 60% cold worked wire can be explained by sub-grain boundary (boundaries less than 2 degrees) formation due to heavy plastic deformation, which had the result of skewing the grain size distribution towards the low side. The average grain size in this wire is likely slightly larger than measured using EBSD. MP35N is highly anisotropic and the crystallographic orientation has an effect on mechanical properties [23]. Figure 3.15 shows the EBSD analysis found MP35N wire with 37% cold work which contains approximately 50% area fraction of <111> oriented grains and 12% area fraction of <100> grains. MP35N wire with 60% initial cold work was found to have slightly higher area fractions of <111> and <100> oriented grains at approximately 52% and 22% respectively. The higher fraction of <100> oriented grains in 60% cold worked MP35N may also explain the lower elastic modulus reported for that wire condition. Previous studies on highly textured MP35N have shown processing conditions that result in a large fractions of <100> oriented grains results in lower elastic modulus values [23]. While it has been shown that preferred orientation in cold drawn MP35N has a significant effect on the mechanical and elastic properties [20], data from the present study showed the main crystallographic texture components remained constant as the

wires were aged. The texture components only changed at temperatures high enough to result in recrystallization.

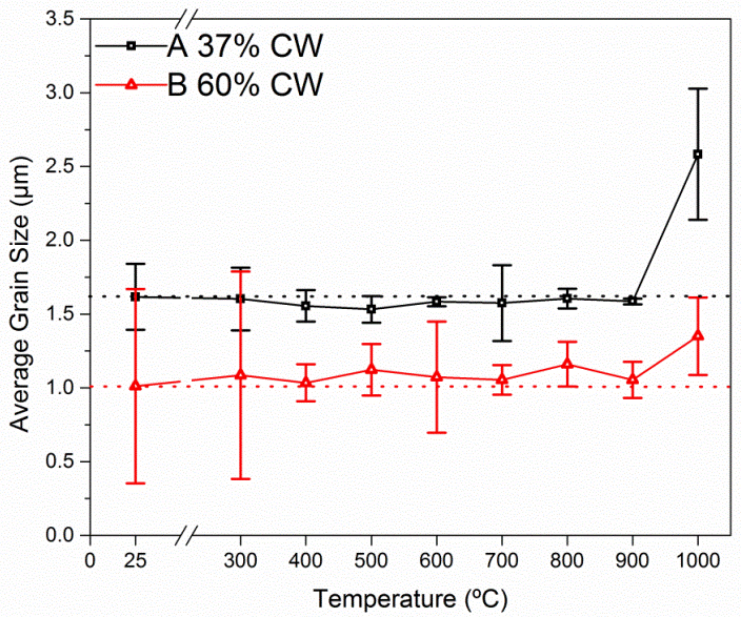

Figure 3.14 – Interval plot showing effect of cold work and heat treatment temperature (60 seconds) on the average grain size MP35N wire. Error bars show three standard deviations from the average [19]. Reprinted with permission from Elsevier.

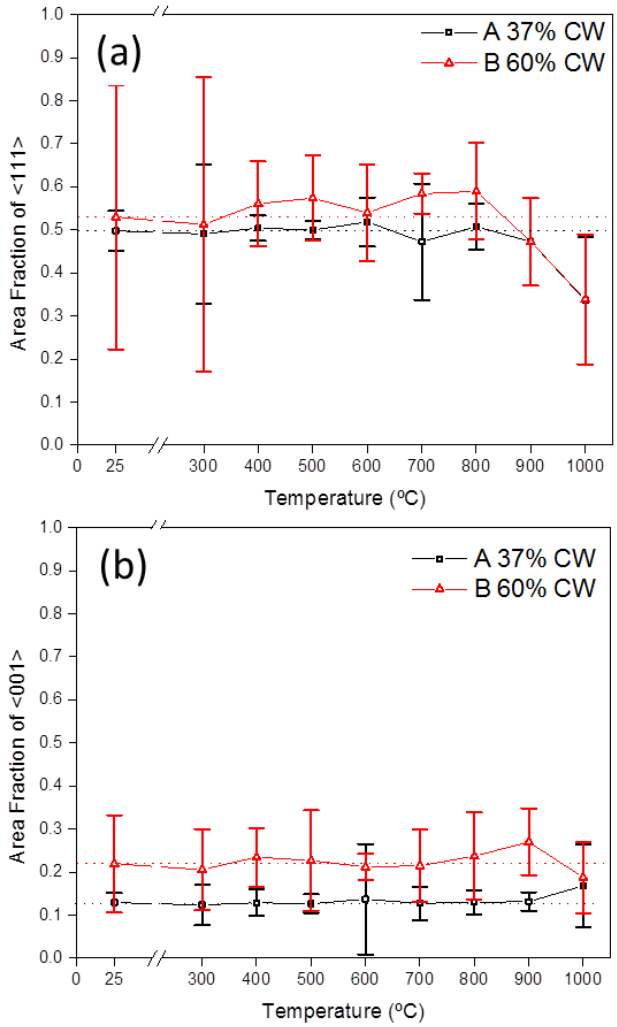

Figure 3.15 - Area fractions of the (a) <111> and (b) <001> texture components in MP35N wire Samples A and B as a function of aging temperature. The error bars correspond to a 95% confidence level [19]. Reprinted with permission from Elsevier.

3.5 CONVENTIONAL TRANSMISSION ELECTRON MICROSCOPY (CTEM)

3.5.1 *LARGE DIAMETER MP35N ROD (3MM)*

3.5.1.1 FULLY ANNEALED MP35N

SEM and EBSD analysis of fully annealed MP35N showed a microstructure consisting of fully large equiaxed FCC grains, annealing twins, and cuboidal titanium nitride particles. Conventional TEM analysis of annealed MP35N rod stock showed similar microstructural features including strain free recrystallized grains, annealing twins, and dislocation loops. While not quantitatively measured, the dislocation density in the fully annealed sample was low. A representative electron micrograph of prismatic dislocation loops punched out from a cuboidal nitride particle found in a sample of fully annealed MP35N imaged using a two beam imaging condition can be found in Figure 3.16. Dissociated partial dislocations were also observed using weak beam dark field (WBDF) or g3g imaging conditions. A bright field/weak beam dark field (BF/WBDF) image pair with the diffraction pattern inset clearly showing a dissociated partial dislocation is shown in Figure 3.17. The right hand region that is visible in Figure 3.17 (b) can be explained by the slightly excited g reflection in the SAD found in Figure 3.17. This reflection was not possible to remove due to local curvature of the sample. The microstructure shown using EBSD and TEM is consistent with a ductile, low strength, low stacking fault energy, face centered cubic metal as shown by hardness testing (Figure 3.1) and literature [24, 25].

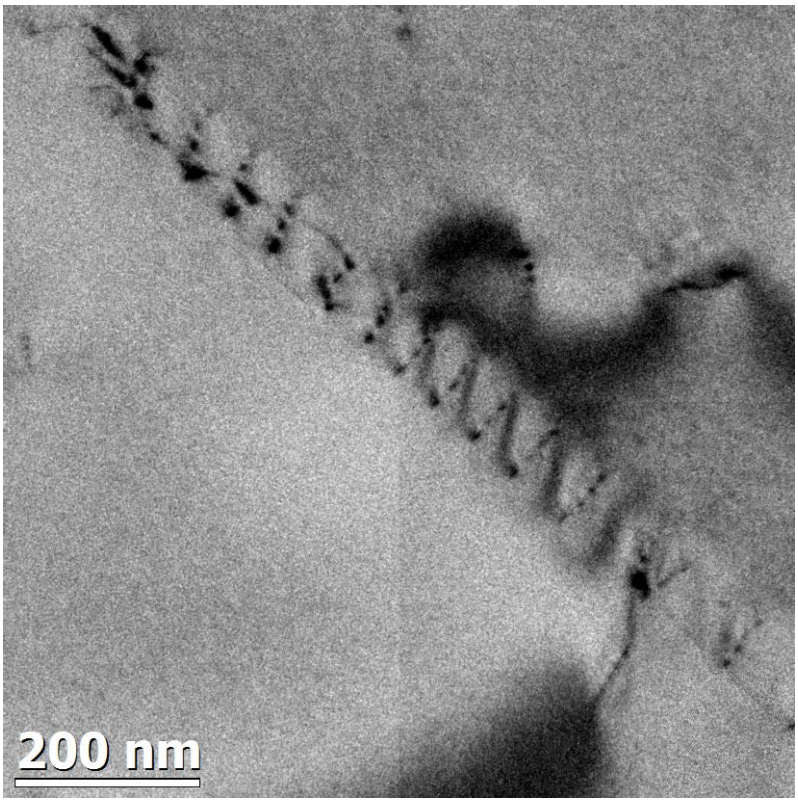

Figure 3.16 – Dislocation loops in a fully annealed and recrystallized MP35N sample.

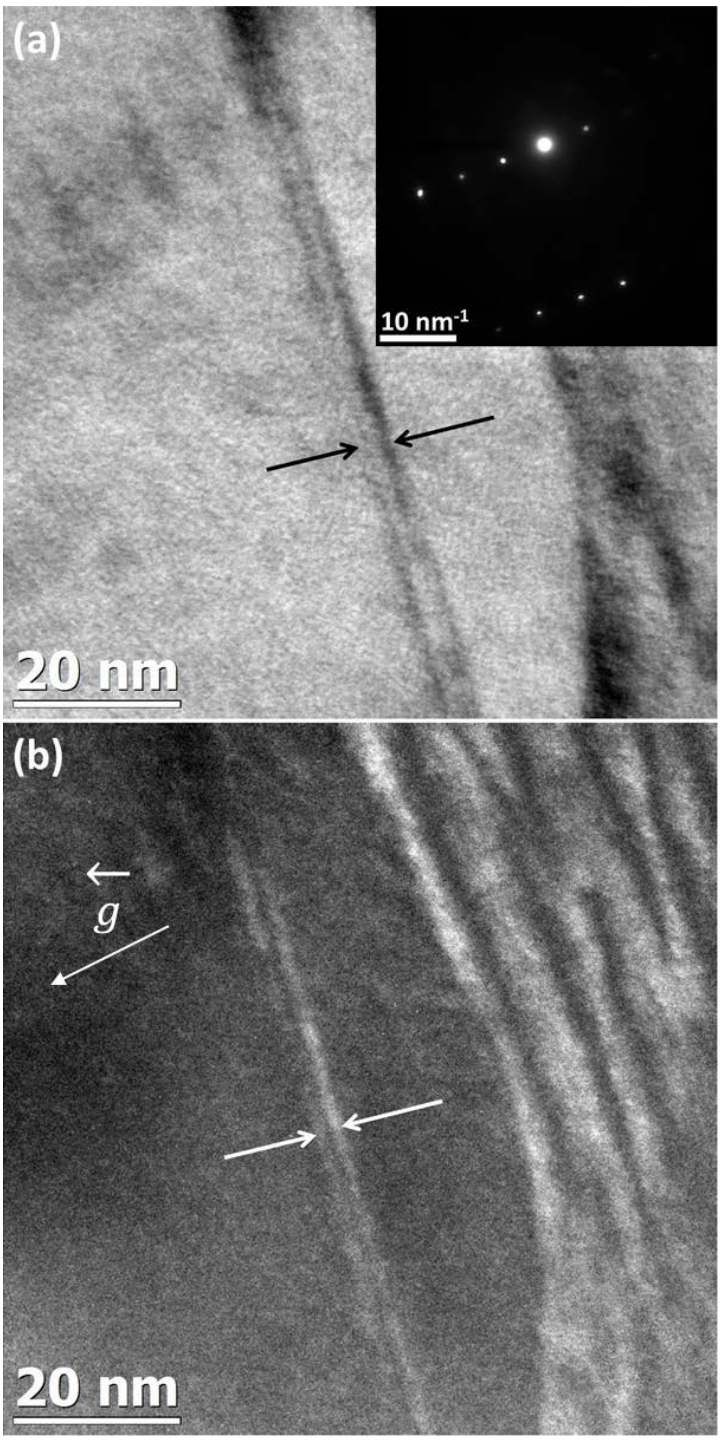

Figure 3.17 - (a) Bright field with selected area diffraction pattern inset and (b) weak beam dark field image of dissociated partial dislocations in fully annealed MP35N. Partial dislocations are highlighted by arrows.

3.5.1.2 25% COLD WORKED MP35N

Following cold drawing to a 25% reduction in cross sectional area, the microstructure consisted of a high density of dislocations and stacking faults with smaller numbers of deformation twins. Both the stacking faults and deformation twins form along <111> habit planes. Figures 3.18 and 3.19 below show representative images of nanotwins and stacking faults, respectively, in a sample of MP35N with 25% prior cold work. The micrographs show microstructural features common to low stacking fault energy (SFE) FCC metals and have been observed by other researchers investigating Co-Fe alloys, MP35N, stainless steel, and brass [26-29]. The plate-like features were determined to be twins by diffraction pattern analysis [30] and bright field/dark field imaging (BF/DF). The BF/DF image pair seen in Figure 3.20 demonstrates the extra diffraction spots correspond to deformation twins in the material.

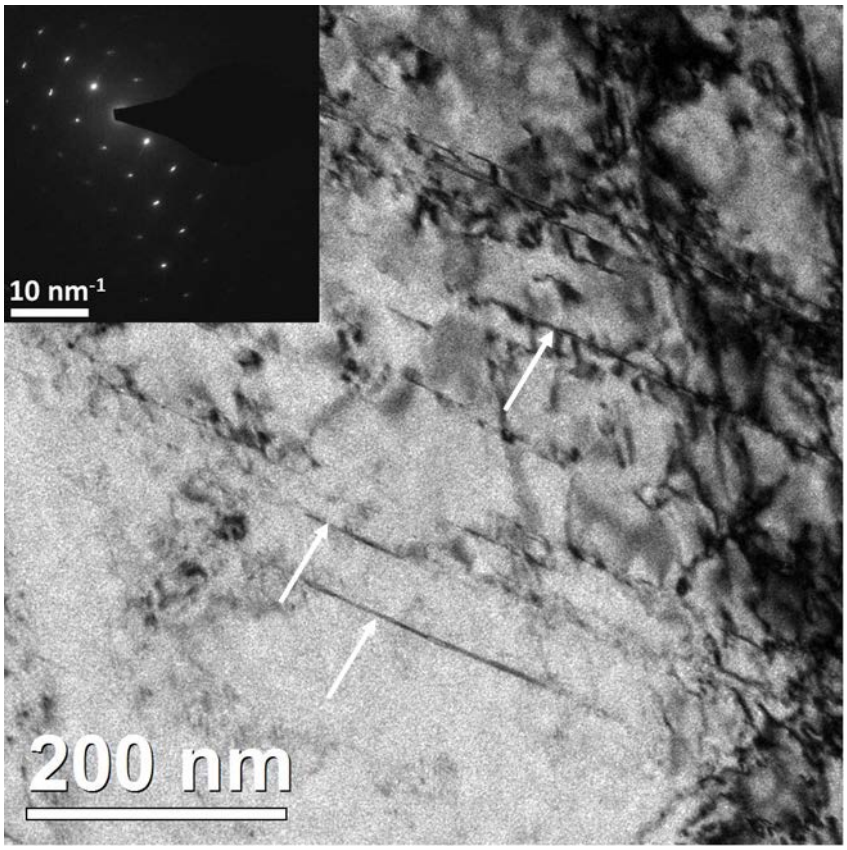

Figure 3.18 – Bright field CTEM image of thin deformation twins formed along <111> planes seen in as-drawn MP35N rodstock following 25% cold work.

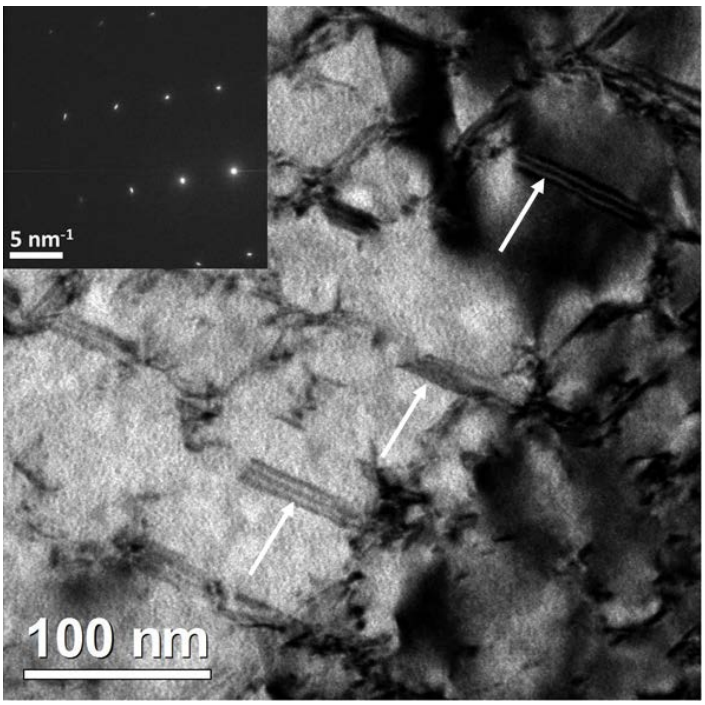

Figure 3.19 – Bright field CTEM image showing stacking fault fringes along <111> planes found in as-drawn MP35N rodstock following 25% cold work.

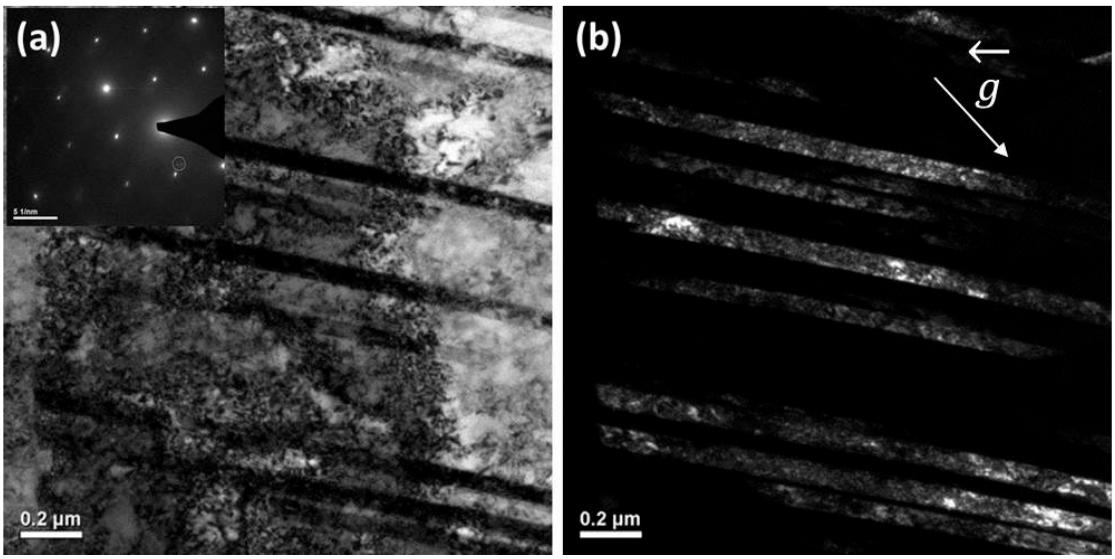

Figure 3.20 – (a) Bright field with selected area diffraction (SAD) pattern inset and (b) dark field taken along the <100> beam direction showing deformation twins in MP35N following 25% cold work.

As reported in previous studies, following thermal treatments, no meaningful changes in the microstructure were observed in cold worked MP35N. The structure remained deformed and the relative number, size, and distribution of deformation twins and stacking faults remained constant at all heat treatment times and temperatures below those required for the onset of recrystallization [9]. Figure 3.21 shows a series of images taken along different zone axes where deformation twins, stacking faults, and dislocation tangles were observed. The microstructure did not appear to change following aging treatments below the recrystallization temperature.

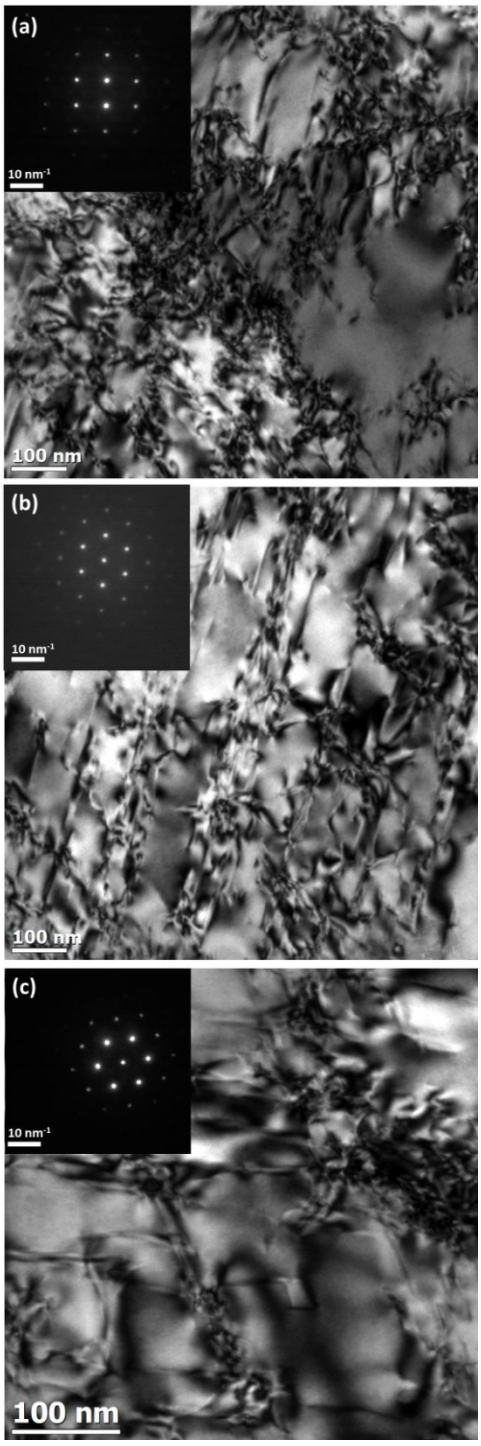

Figure 3.21 – Bright field TEM images showing the microstructure of 25% cold worked MP35N following a thermal treatment at 700°C for 5 minutes (a) oriented along a <100> zone axis, (b) oriented along a <110> zone axis, and (c) oriented along a <111> zone axis.

3.5.1.3 48% COLD WORKED MP35N RODSTOCK

MP35N rod stock with 48% cold work showed a similar microstructure to the previously shown 25% cold worked material. The most notable difference is the qualitative volume fraction increase in deformation twins and dislocation tangles. Selected area diffraction analysis was unable to detect phases other than FCC (Figure 3.22). Extra diffraction spots were identified as deformation twins or double diffraction in agreement with previous research [15, 16]. As in the case of 25% cold worked MP35N, no changes in microstructure or phases present were observed following aging at 600°C for 30 minutes Figure 3.23. The plate-like features were still identified as deformation twins as observed in the as drawn material.

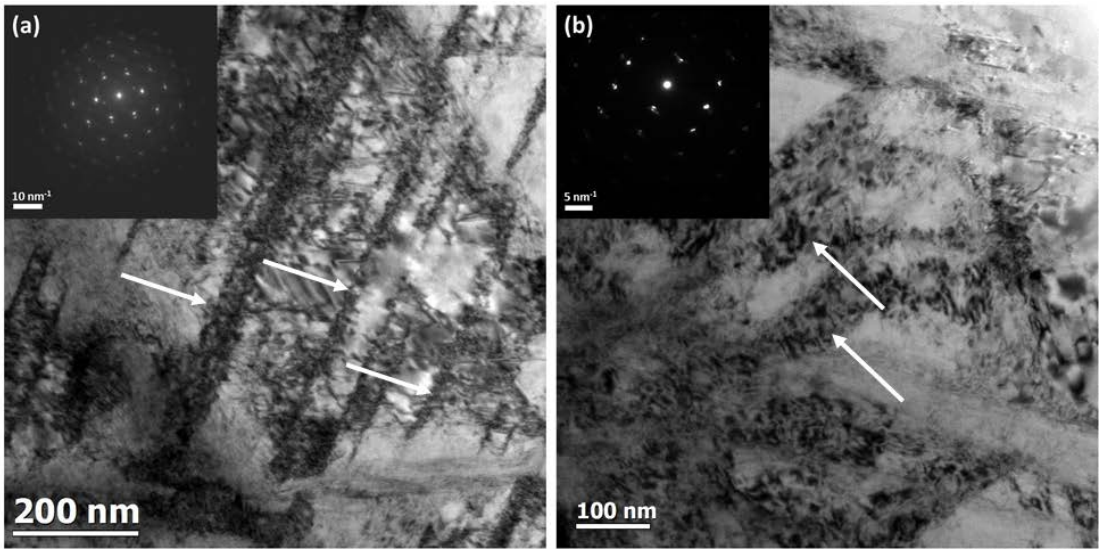

Figure 3.22 - Bright field CTEM images of MP35N rod stock with 48% cold work showing a microstructure consisting of FCC grains and deformation twins near the (a) <110> and (b) <112> zone axes.

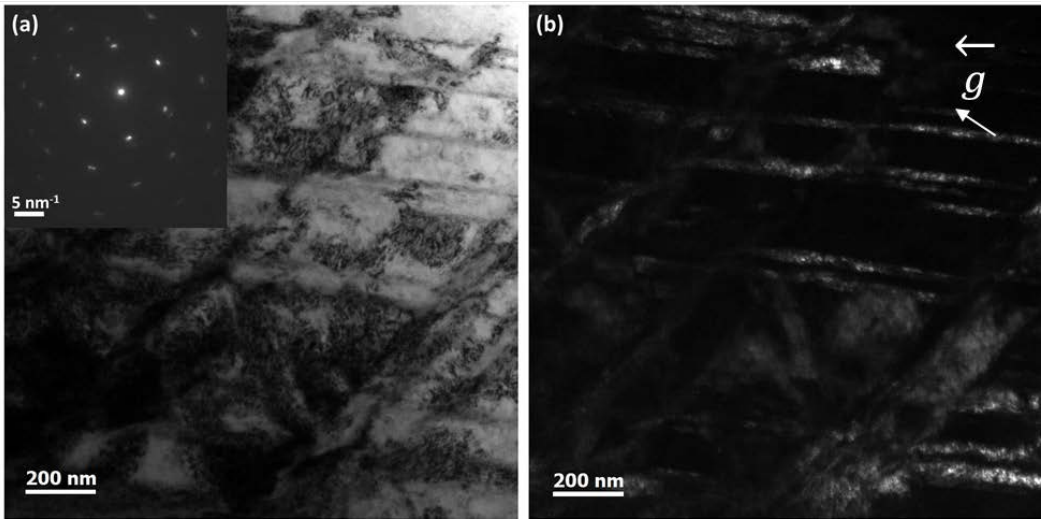

Figure 3.23 - (a) Bright field (b) dark field pair MP35N rod stock with 48% cold work following aging at 600°C for 30 minutes showing a microstructure consisting of only FCC grains and deformation twins [19]. Reprinted with permission from Elsevier.

3.5.2 *MP35N WIRE (178 µM DIAMETER)*

3.5.2.1 MP35N WIRE AGED AT 700°C FOR 60 SECONDS

The increased mechanical strength observed in MP35N in the 37% cold drawn and aged condition is of a magnitude not commonly observed in other material systems where age hardening occurs. In the case of 37% cold worked MP35N aged at 700°C for 60 seconds, there is a 15% increase in the ultimate tensile stress and 21% increase in the offset yield stress compared to the as drawn wire. In other alloys that age harden such as 6000 series aluminum alloys, nickel-based super alloys, precipitation hardening steels, and copper-beryllium alloys typically precipitate second phases which act as barriers to dislocation motion. In general, the phases that precipitate from solution have a different crystal structure and can be detected using x-ray and electron diffraction techniques. In contrast to these materials, careful TEM and electron diffraction analysis

of peak aged MP35N wires with an ultimate tensile strength on the order of 2.1 GPa showed a microstructure consistent with the bulk rodstock samples discussed in previous sections. Figure 3.24 shows a representative images of 37% cold worked MP35N aged for 60 seconds at 700°C where only deformation twins and dislocations are present. The inset diffraction pattern in Figure 3.24 only contains spots that correspond to the matrix and deformation twins.

A similar low magnification image of deformation twins in a single grain of MP35N wire can be seen in Figure 3.25(a). Slight adjustments to the sample tilt to align the specimen along a zone axis results in a high resolution image of the twin, which is shown in Figure 3.25(b). The image and the corresponding fast Fourier transform (FFT) clearly demonstrate the plate-like features to be deformation twins and not precipitates.

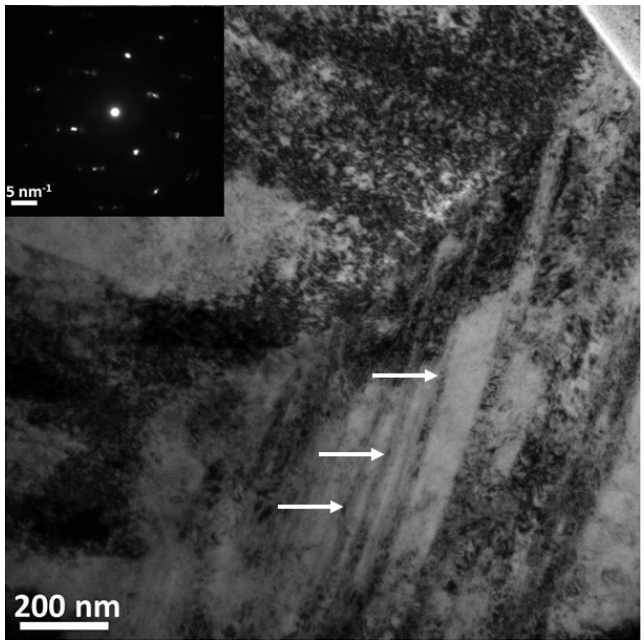

Figure 3.24 – Bright field CTEM image of MP35N wire with 37% cold work aged for 1 minute at 700°C with selected area diffraction pattern inset. The microstructure consists of fine deformation twins and dislocations.

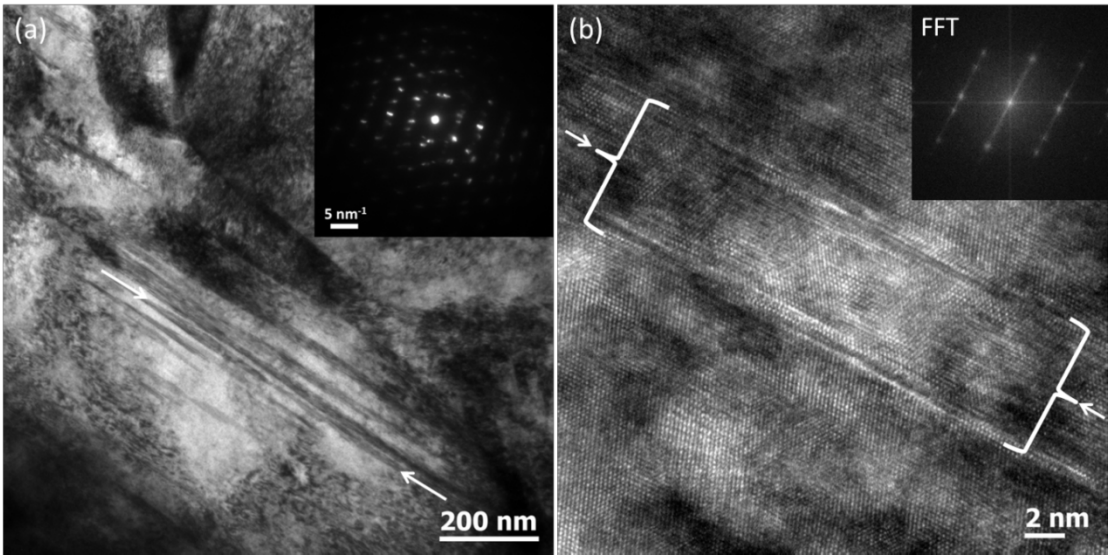

Figure 3.25 - (a) Low-magnification and (b) high-magnification BF-TEM images of deformation twins in MP35N wire with 37% prior cold work (sample A) aged at 700°C for 60 seconds. The inset in (a) is a SAD pattern obtained from the sample and the inset in (b) is a fast Fourier transform (FFT) of the image showing the presence of deformation twins [19]. Reprinted with permission from Elsevier.

3.5.2.2 MP35N WIRE AGED AT 900°C FOR 60 SECONDS

After the large increase in mechanical strength up to the peak aging conditions, a second interesting observation was made during mechanical testing of cold drawn and aged MP35N wires. The apparent onset of recovery and subsequent decrease in strength after aging the wires at temperatures above 700°C is not accompanied by an increase in uniform elongation. During recovery, enough energy is added to the system to allow the annihilation of dislocations and other defects resulting in incremental increases in ductility as barriers to dislocation motion disappear [31]. The samples of MP35N containing 37% cold work and aged for 60 seconds at 900°C showed this behavior as seen in Figure 3.2 and Figure 3.5. As with all other rod stock and wire conditions examined using conventional TEM analysis in this study, no unusual

microstructural features could be found. Figure 3.26 shows a representative bright field TEM image of 37% cold worked MP35N aged for 60 seconds at 900°C where a large number of stacking faults (highlighted by white arrows) can be seen. In many locations of the sample, the high concentration of deformation twins found in other processing conditions were not observed in certain grains, as seen in Figure 3.26. No quantitative analysis on the density of deformation twins was performed, but the qualitative difference in defect density may explain the decrease in yield stress observed in tensile test samples of wire aged at 900°C for 60 seconds. Further analysis of the sample did reveal locations with high densities of deformation twins and dislocations as seen in Figure 3.27 and 3.28. Also worth noting is the dislocation substructure found within the deformation twins revealed in the dark field images of Figure 3.27. The observation of dislocations within deformation twins and confined by the twin boundaries is further evidence that micro- and nanotwins are effective barriers to dislocation motion.

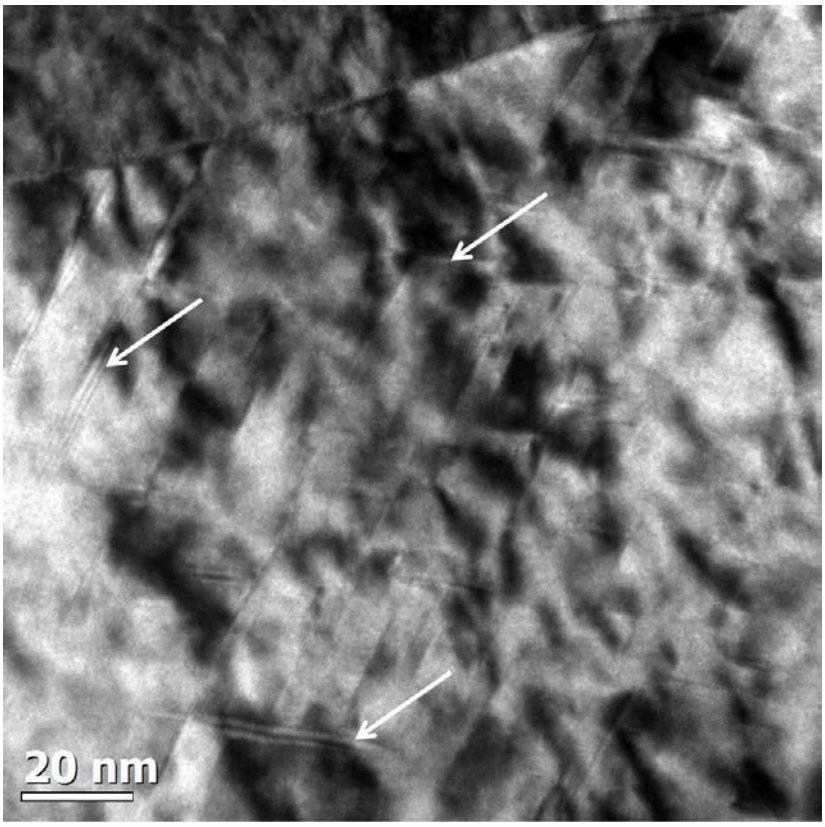

Figure 3.26 – BF-TEM image of stacking faults in MP35N wire with 37% cold work following aging at 900°C for 60 seconds. Stacking faults are highlighted by white arrows.

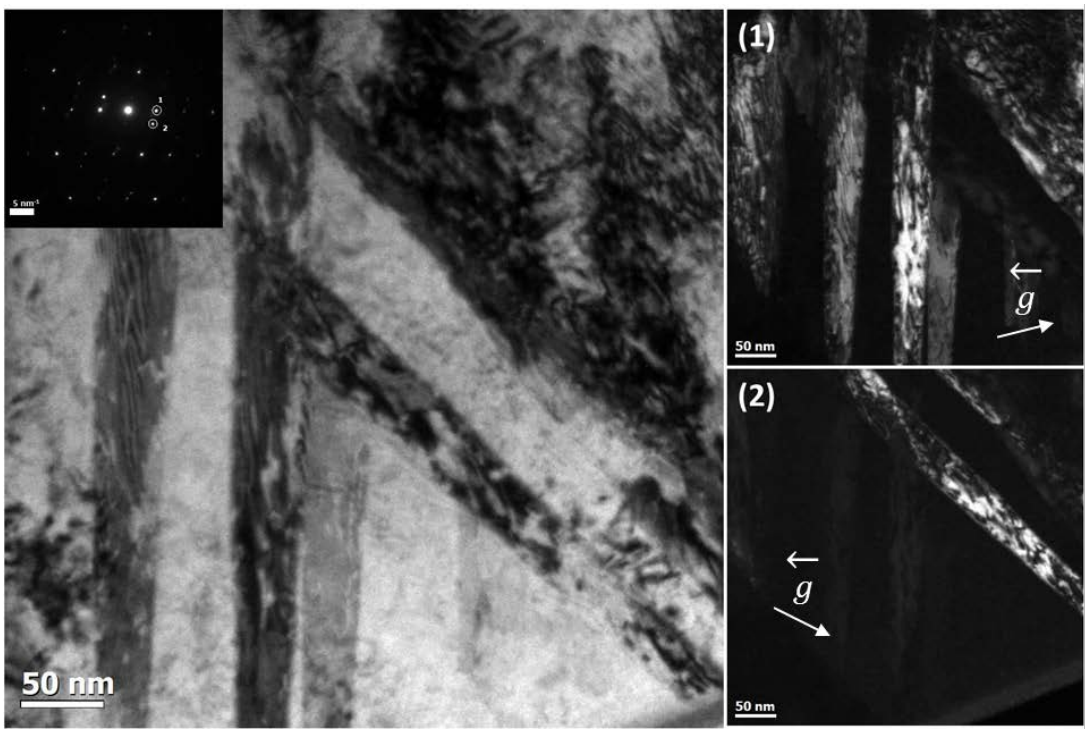

Figure 3.27 – BF-TEM image with corresponding SAD pattern inset of deformation twins in 37% cold worked MP35N following aging at 900°C for 60 seconds. The dark field images on the right highlight both variants of the twins in the bright field image.

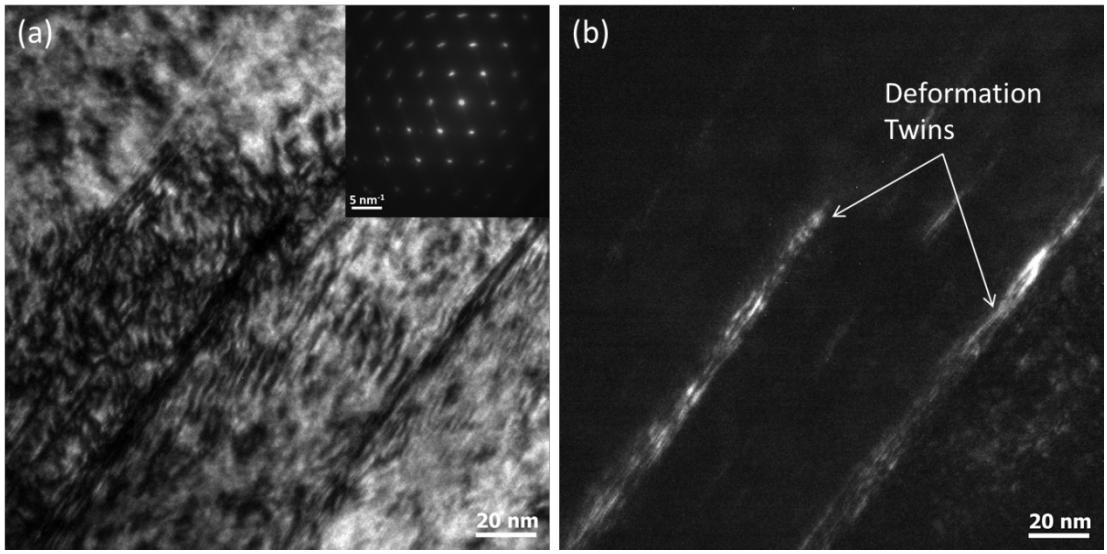

Figure 3.28 – BF/DF TEM pair of images highlighting deformation twins in 37% cold worked MP35N aged at 900°C for 60 seconds.

3.5.3 *ENERGY FILTERED TEM (EFTEM)*

In the above experiments, selected area diffraction analysis and dark field imaging was used to characterize the microstructure of as drawn rod stock and cold worked MP35N rod stock and wire. While conventional TEM imaging and diffraction is a powerful tool for microstructural characterization, no changes in the microstructure such as precipitation reactions or phase transformations were detected. This finding is consistent with contemporary literature pertaining to MP35N [14, 16] but could not pinpoint the mechanism of secondary hardening observed upon aging cold worked MP35N. In order to analyze the local chemistry of cold worked and aged MP35N energy filtered transmission electron microscopy (EFTEM) was utilized.

EFTEM has many advantages over conventional TEM imaging including improved resolution and contrast, thickness mapping in terms of electron mean free path, and

compositional information by filtering out ionization edge energy ranges of interest [32]. Figure 3.29 below shows a comparison of a deformation twin HRTEM image taken with and without zero loss energy filtering. The zero loss filtered image shows improved contrast and resolution.

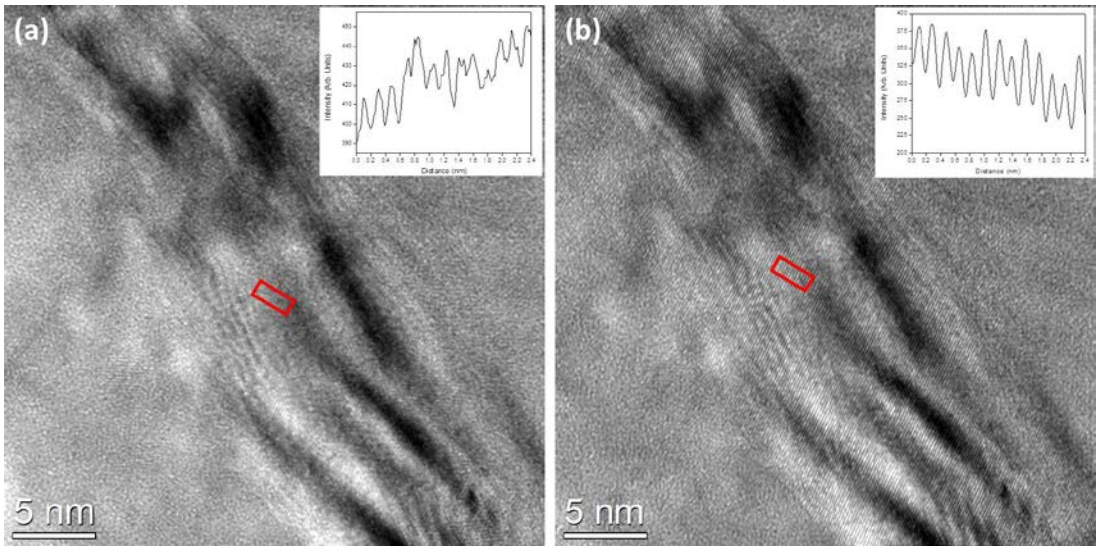

Figure 3.29 – Comparison of HRTEM images of a stacking fault in as drawn 48% cold worked MP35N comparing (a) standard bright field image and (b) zero loss filtered image. The inset intensity profiles show the increase in resolution and reduction in noise that zero loss image filtered imaging allows.

Since the Mo $M_{4,5}$ edge EELS signal has a delayed peak and is relatively featureless, the Ni and Co $L_{2,3}$ edges were used for energy filtering [33]. The results are presented in Figure 3.30. As can be seen, the zero-loss EF-TEM image contains regions of low contrast that correspond to deformation twins. It also shows that the intensity of the combined Ni and Co $L_{2,3}$ edges was reduced at the twins by about 5 to 10% and was slightly higher in adjacent regions, suggesting segregation occurs at the deformation twins.

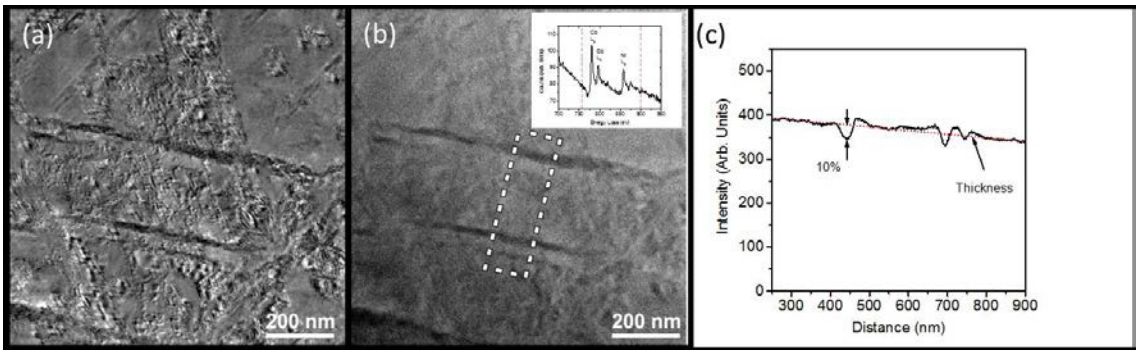

Figure 3.30 - EF-TEM images of MP35N with 48% cold work, aged at 600°C for 30 minutes (sample E) obtained using (a) zero-loss and (b) core-loss with 755 eV to 890 eV energy window containing Co and Ni $L_{2,3}$ edges. The inset in (b) is the core-loss window used in (b). (c) The intensity of the combined Co and Ni $L_{2,3}$ edge EELS edges computed from the rectangular area shown in (b). The overall intensity reduction due to specimen thickness is indicated by the black line [19]. Reprinted with permission from Elsevier.

3.6 ANALYTICAL SCANNING TRANSMISSION ELECTRON MICROSCOPY (STEM)

Following the observations in the EFTEM experiments suggesting local segregation, further experimentation was undertaken to determine if the strengthening of cold worked MP35N upon aging is a result of local chemical changes as opposed to the more commonly observed microstructural and phase changes in other alloys. The lack of clear evidence for second phase precipitation as a strengthening mechanism for MP35N in previous studies resulted in an alternate mechanistic explanation for the observation of secondary hardening. Asgari et al. [10] had proposed Suzuki segregation, or preferential segregation of solute atoms to thin HCP platelets within the matrix causing coarsening of the thin HCP phases.

As previously stated, in the current study no qualitative differences in defect density including stacking faults and twins, was observed following aging conditions below the recovery and recrystallization temperatures. The relative number of stacking faults and deformation twins, although approximately constant, was large especially in the samples containing 48% to 60% cold work. Representative bright field scanning transmission electron (BF-STEM) images of samples containing large area fractions of deformation twins and stacking faults in cold worked MP35N are shown in Figure 3.31. Even in conditions with less severe cold work, large numbers of intersecting deformation twins have been observed.

Standard BF- STEM imaging yields similar information to a bright field conventional TEM image. Even further characterization power for STEM imaging is realized when annular dark field (ADF) or high angle annular dark field (HAADF) imaging conditions are utilized. Medium angle annular dark field (ADF) microscopy images using electrons scattered at intermediate angles [34, 35] which are most sensitive to localized strains at interfaces [36] and precipitates [37], and is thus referred to as strain contrast imaging. HAADF images are formed using electrons scattered inelastically at high angles and can yield atomic number contrast. HAADF of cold worked and aged MP35N revealed high contrast at stacking faults and deformation twins. The contrast in a HAADF image may be a result of a higher average atomic number, sample thickness, sample preparation induced surface amorphous layer, or local crystal strain [38-40]. Figures 3.32 and 3.33 show the contrast differences observed in aged MP35N in two prior cold work conditions. In all cases the contrast difference is clear between the fault/twin and the matrix.

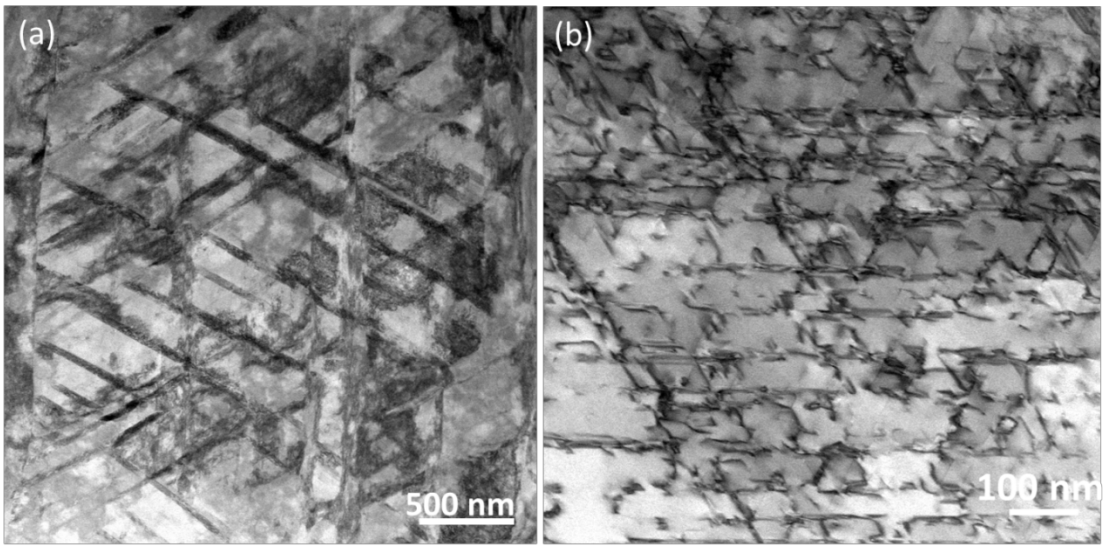

Figure 3.31 – Low-magnification BF-STEM images showing high area fractions of stacking faults in (a) 25% cold-worked MP35N rod aged for 30 minutes at 600°C (sample D) and deformation twins in (b) 48% cold-worked MP35N rod aged for 30 minutes at 600°C (sample E) [19]. Reprinted with permission from Elsevier.

The preferential segregation of HCP stabilizing elements, and subsequent expulsion of FCC stabilizing elements from stacking faults and twins could not be conclusively shown using HAADF imaging alone as the contrast is not only related to atomic number but other possible factors. For this reason EDS line scans were performed to quantify the concentration of elements starting in the matrix. EDS scans across the stacking faults and twins that showed high contrast in HAADF images were performed. Figure 3.34 shows an EDS line scan across a dissociated dislocation with the accompanying HAADF image showing what appears to be Z contrast in a 25% cold worked MP35N rod heat treated at 600°C for 30 minutes. The line scan shows increased molybdenum concentration and a decrease in nickel and cobalt concentrations approximately

consistent across the partial dislocation. This observation is consistent with the driving force for Suzuki segregation of HCP stabilizing elements to the fault and rejection of FCC stabilizing elements. Interestingly, the chromium concentration remained approximately consistent across the partial dislocation.

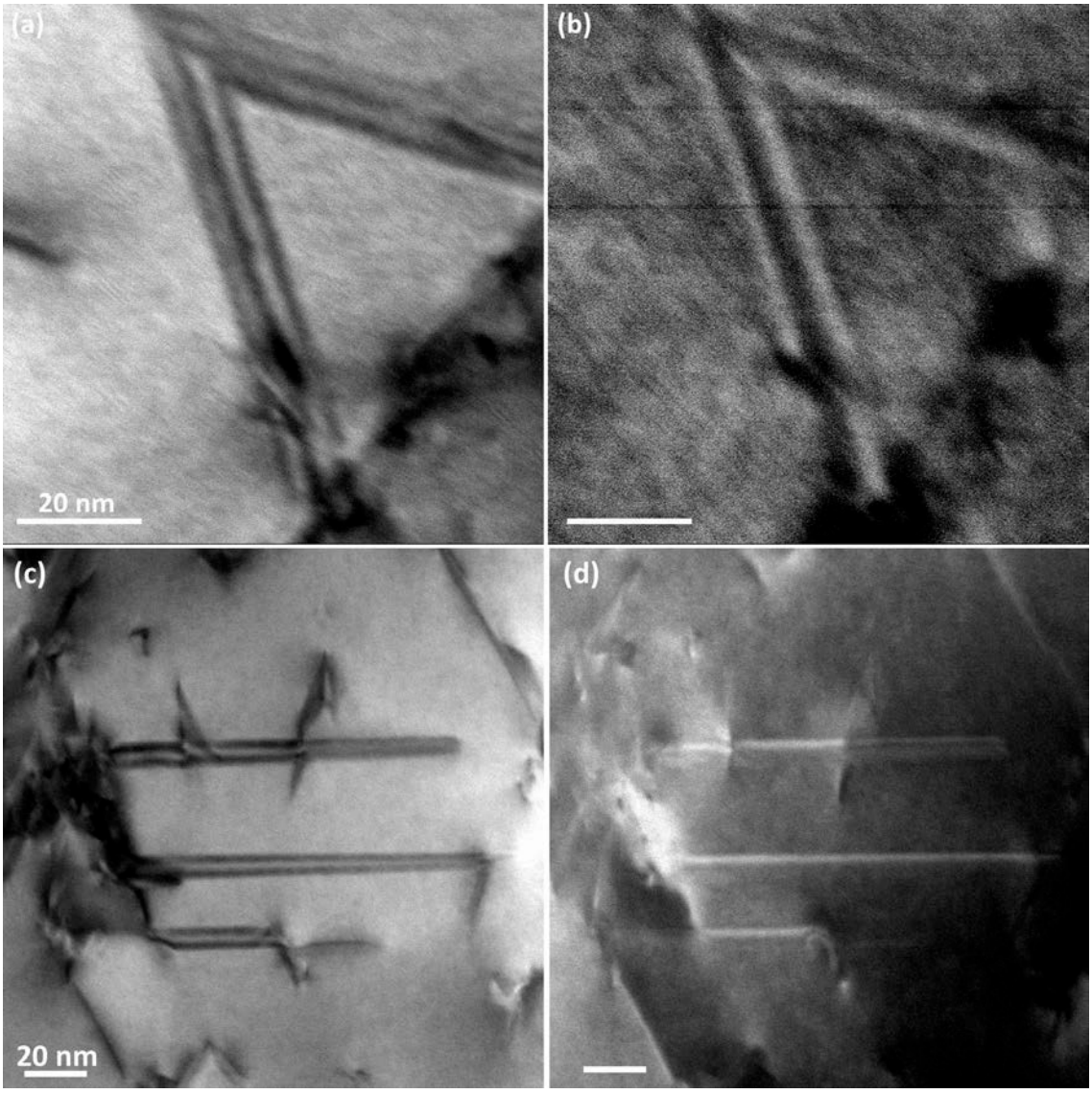

Figure 3.32 – (a,c) BF and (b,d) HAADF-STEM images showing stacking faults in MP35N rod with 25% cold work (sample D) aged at 600°C for 30 minutes. The higher contrast in the stacking faults seen in the HAADF-STEM images indicates the presence of heavier elements.

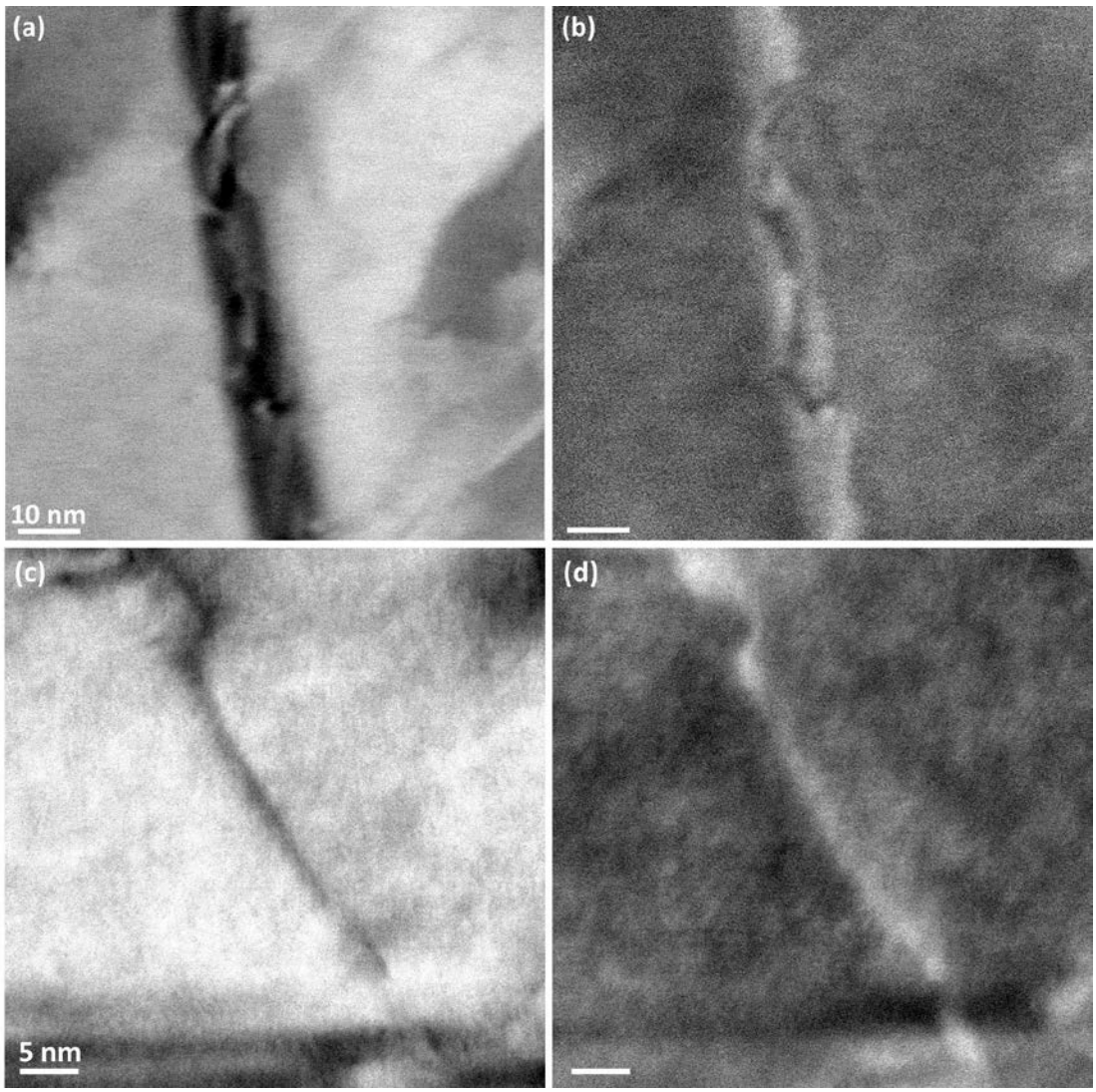

Figure 3.33 – (a,c) BF and (b,d) HAADF-STEM images showing deformation twins and stacking faults in MP35N rod with 48% cold work (sample E) aged at 600°C for 30 minutes. The higher contrast in the stacking faults seen in the HAADF-STEM images indicates the presence of heavier elements [19]. Reprinted with permission from Elsevier.

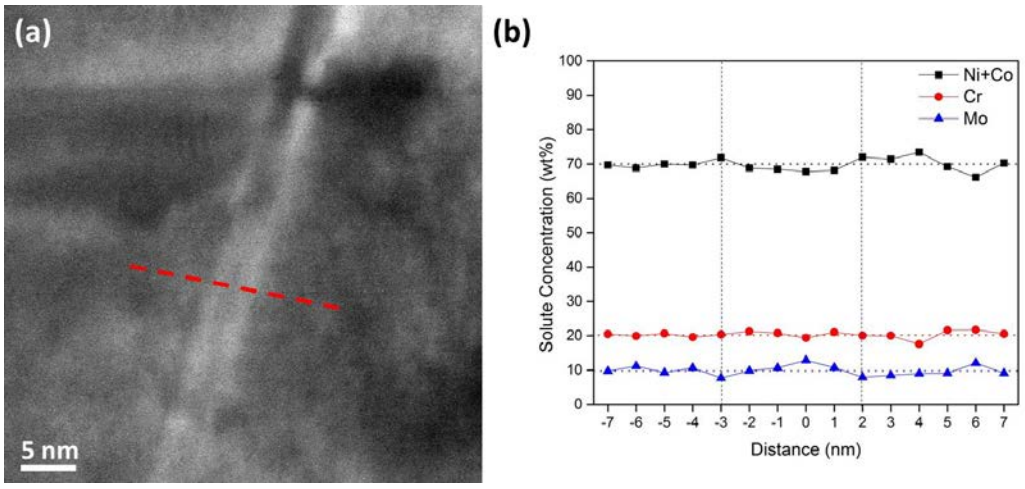

Figure 3.34 – (a) HAADF-STEM image of dissociated partial dislocations in 25% cold worked MP35N rod heat treated at 600°C for 30 minutes (b) EDS line scan showing local molybdenum enrichment and nickel + cobalt depletion across the partial dislocations.

Similarly, EDS line scans were performed on 48% cold worked and aged MP35N rod aged at 600°C for 30 minutes. The trend of molybdenum enrichment at stacking faults and deformation twins and depletion of nickel and cobalt was consistent with the previous material condition. The local chemical analysis of aged MP35N with different amounts of initial cold work also showed the amount of molybdenum enrichment increased proportional to the prior dislocation density. A possible mechanism for this observation will be explored in the discussion section.

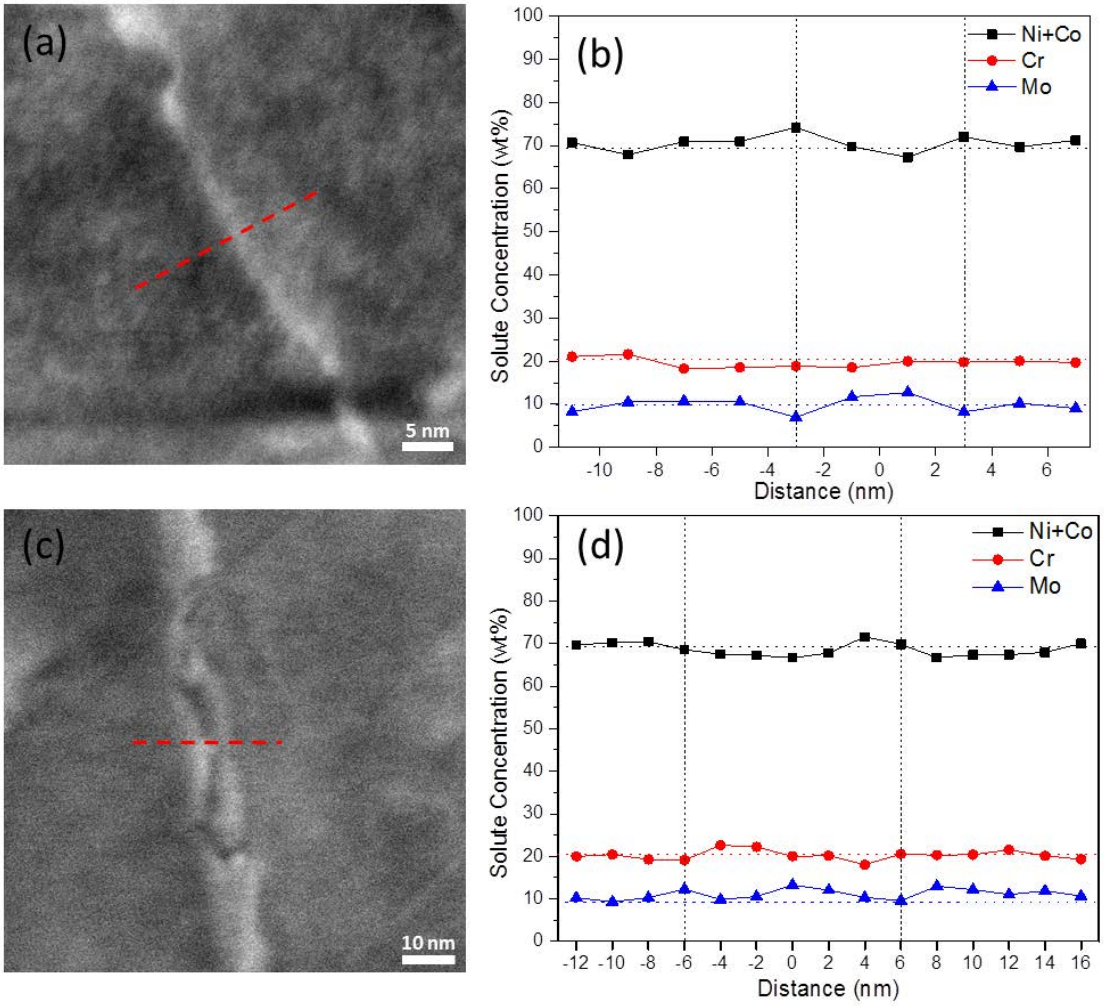

Figure 3.35 – (a,c) HAADF-STEM images of a stacking fault (a) and deformation twin (c) in 48% cold worked MP35N heat treated at 600°C for 30 minutes (b,d) corresponding EDS line scans showing local molybdenum enrichment and nickel + cobalt depletion across the stacking fault and twin.

Finally, to confirm the enrichment of molybdenum is a result of the aging process, a series of EDS point scans were performed on stacking faults and twins from 48% cold worked MP35N in the as drawn condition. The as drawn samples with no aging showed lower contrast at deformation twins and stacking faults when imaged under HAADF

conditions. Figure 3.36 shows representative BF and HAADF-STEM images of a stacking fault and deformation twin in 48% cold worked MP35N in the as-drawn condition (no aging). In the case of the deformation twin seen in Figure 3.36 (d), bright contrast is observed in the HAADF image. As discussed above, high contrast in annular dark field images may be a result of local chemistry changes, sample thickness, or microstructural strain. EDS scans on multiple stacking faults and deformation twins were collected and compared with the matrix in the immediate vicinity of the defects. The results of the spots scans from as-drawn MP35N with no aging treatment, shown in Figure 3.37, shows no statistical difference between the chemistry of stacking faults and deformation twins and the bulk material in cold worked MP35N prior to aging.

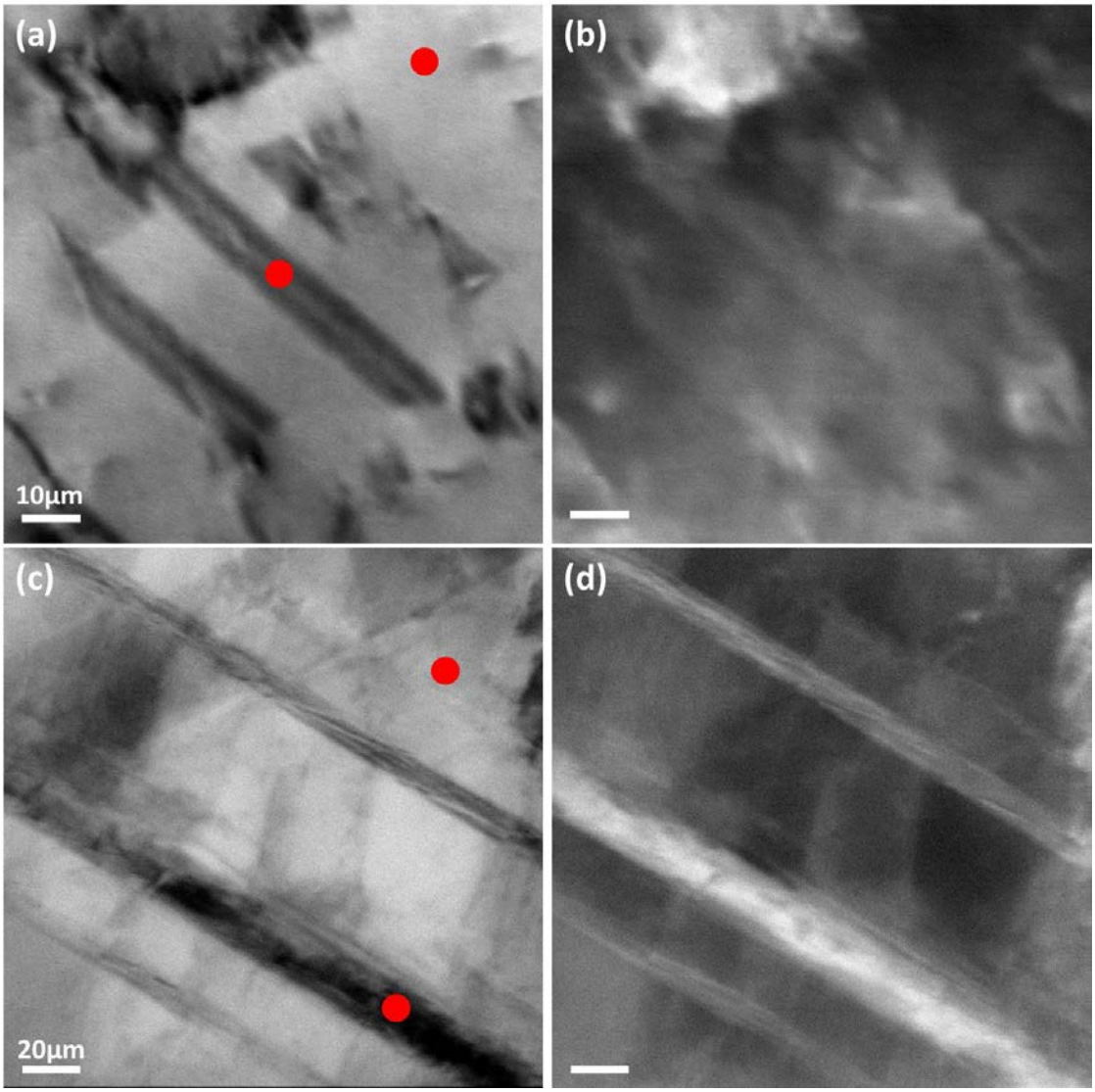

Figure 3.36 – (a) Bright field and (b) HAADF-STEM images of a stacking fault in 48% cold worked MP35N rod in the as-drawn condition (no aging treatment). Unlike the HAADF images seen in aged MP35N rod, the stacking fault shows low contrast compared to the matrix. (c) BF-STEM and (d) HAADF-STEM images showing a deformation twin in 48% cold worked MP35N rod. EDS scan locations are shown as red dots on the BF-STEM images.

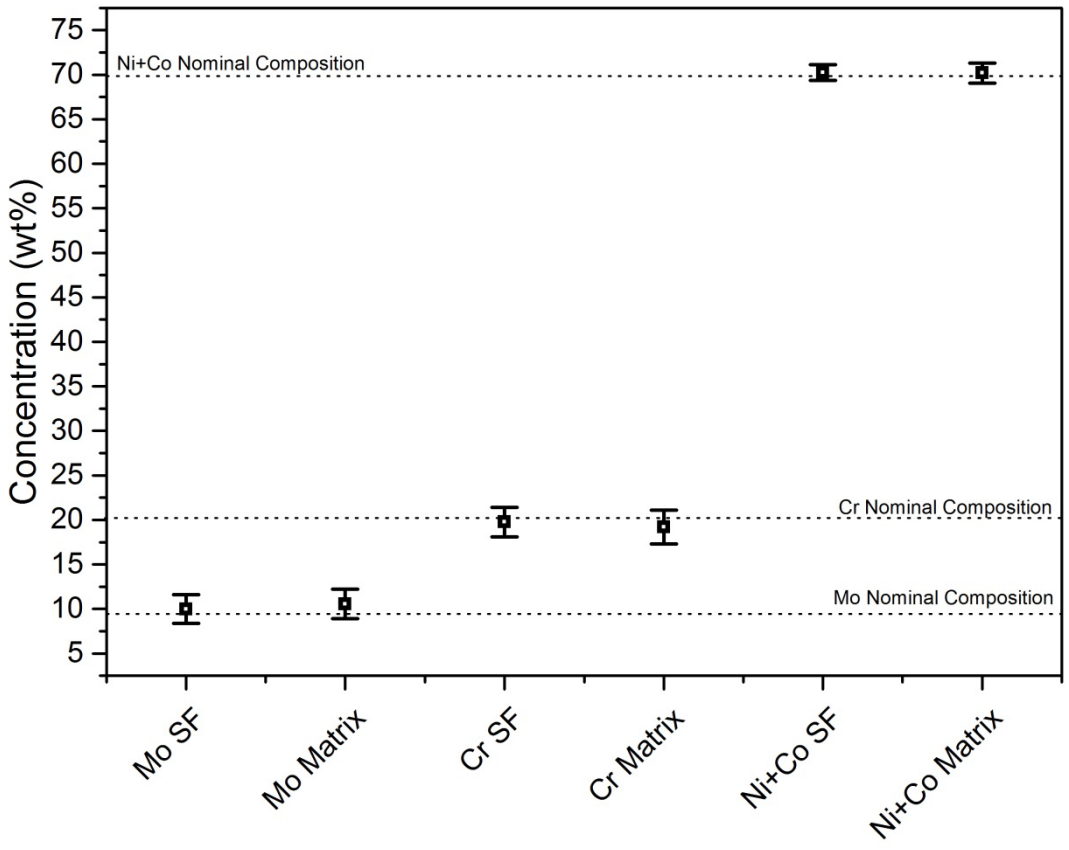

Figure 3.37 – Interval plot comparing chemistry at stacking faults and deformation twins to the matrix for each major component in MP35N with 48% cold work prior to aging. The dotted lines signify the nominal composition determined by analytical chemistry. The sample size was n=6 and the error bars signify a 95% confidence interval.

4 DISCUSSION

The significant hardening observed in MP35N following relatively brief aging cycles and a wide range of temperatures is unusual. Precipitation hardening nickel based superalloys such as Inconel and Waspaloy are commonly used in applications where strength is required at high temperatures. These alloys were designed to precipitate out gamma prime (γ′) phase from a saturated solid solution. MP35N is a four component, single phase FCC alloy with low concentrations of interstitials or other elements such as iron or titanium. Although historical studies on the microstructure of cold worked and aged MP35N reported the presence of HCP martensite or Co_3Mo precipitates [7], contemporary studies, including this work, have found the microstructure to consist of deformation twins and stacking faults in the cold worked and aged condition [14, 16]. Metallic materials in general do not undergo strengthening upon aging without precipitation of new phases from a saturated solid solution as observed in MP35N. Furthermore, in order for traditional aged hardening alloys to precipitate second phases the material must be heat treated at a high enough temperature to solutionize the material, which in many cases causes the material to recrystallize. MP35N behaves differently in both respects. MP35N does not show signs of secondary phases, including hexagonal martensite, when analyzed in the aged condition and the secondary hardening does not occur in the solution annealed condition. The observation that a prior dislocation density is required for MP35N to age harden has been reported previously [9] and was shown in the results of microhardness testing as seen in Figure 3.1. MP35N, as a low stacking fault energy metal, readily forms stacking faults and deformation twins while undergoing plastic flow. The results of this study have shown solute elements that stabilize HCP phases (a stacking fault in an FCC metal is a thin

HCP layer) preferentially accumulate at faulted regions while FCC stabilizing elements are rejected into the matrix. This phenomena, known as Suzuki segregation [12], has been reported in other low stacking fault energy materials such as Cu-Sn alloys [41], Mg-Zn-Y alloys [42], Ni-Co based superalloys [43], γ′ precipitates in Ni based superalloys [44], and other members in the "MP" family of alloys [45]. The results of this study agree with aforementioned Ni-Co studies in the observation of Mo segregation, however it has been reported elsewhere both experimentally [44] and theoretically [43] that increases in Co and Cr at stacking faults occurs in addition to the changes in Mo and Ti depending on the alloy composition. Further phase field modeling work on the specific chemistry of MP35N would be required to understand this discrepancy as the model reported by Koizumi et al. [43] shows the elements that segregate to stacking faults are strongly dependent on the minor alloying additions to the material [43]. The results of this study also showed the amount of prior cold work and resulting dislocations, deformation twins, stacking faults, and larger non-equilibrium vacancy concentration in the material is proportional to the magnitude of secondary hardening. The EDS data collected was also able to demonstrate that the amount of molybdenum segregation also increases as the amount of prior cold work increases compared with the matrix as shown in Figure 4.1.

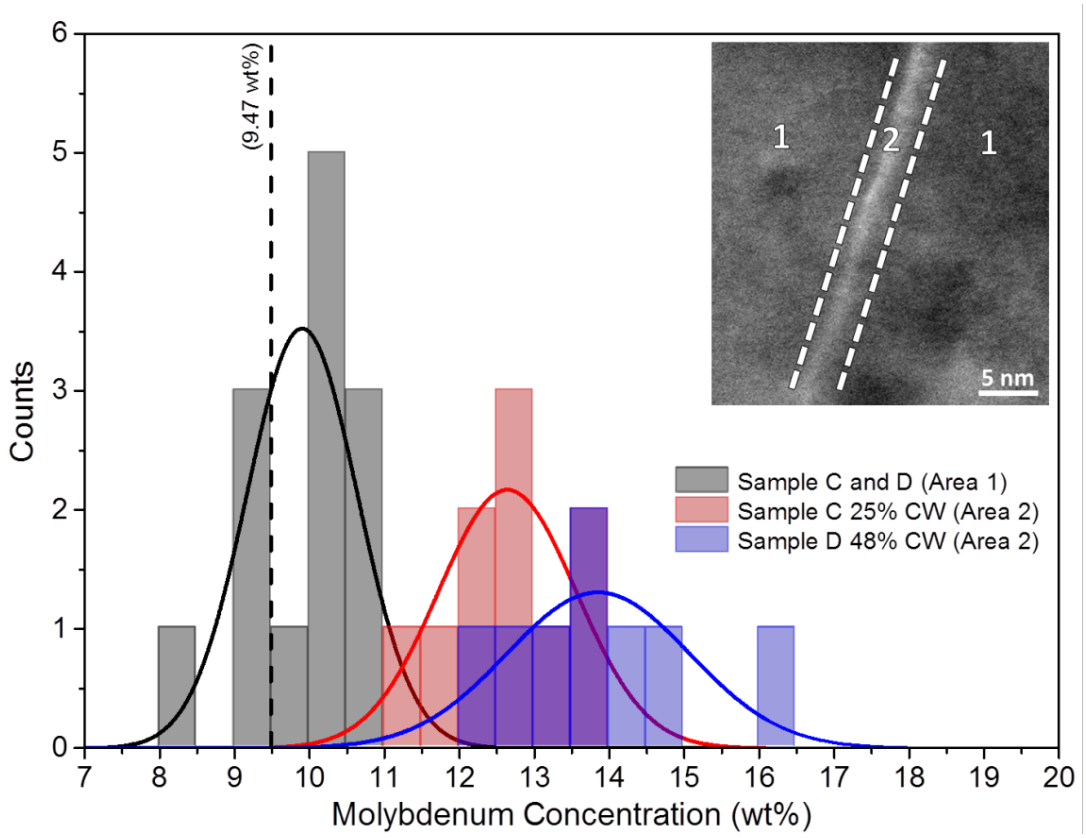

Figure 4.1- Histograms of Mo concentrations at the stacking faults and deformation twins in MP35N rod (samples C and D). The histogram of Mo concentrations obtained from the matrix, away from faults and twins, is also shown. The inset is a HAADF-STEM image of a deformation twin with highlighted typical regions from where data for histograms are obtained [19]. Reprinted with permission from Elsevier.

The most interesting result of the Suzuki segregation observation in MP35N is the significant changes in mechanical properties that occur following brief aging cycles on the order of seconds. The increases in mechanical strength and elastic modulus coupled with a rapid loss in ductility following a brief aging treatment of cold worked MP35N warrants further discussion. MP35N is a quaternary single phase alloy with reasonable solid solution strengthening in the fully annealed condition when compared to Ni-Cu, 5000 series aluminum alloys, and Cu-Be alloys. Cold working MP35N results in large volumes of deformation twins and dislocation pileups that significantly strengthen the material compared with the solution annealed condition [46]. Interestingly, the elastic modulus decreases in MP35N following heavy cold work from approximately 230 GPa to values ranging from 150 GPa to 190 GPa. A similar phenomena has been reported for iron that has been deformed in tension but the magnitude of the modulus drop was on the order of 7% [47], much less than the 17% to 35% decrease found upon cold drawing MP35N. This has also been reported by others using nanoindentation techniques and traditional tension testing [48, 49]. The strong change in crystallographic orientation from the random texture distribution in the fully annealed condition to the strong <111> texture observed following cold drawing likely plays a significant role in the decreased elastic modulus as MP35N has been reported to be highly anisotropic [23]. The gradual increase in elastic modulus as the wire is aged is of more interest. No changes in microstructure or crystallographic texture were observed as the cold worked material was aged making the increase in elastic modulus more likely to be related to the local chemistry changes observed at crystal defects, which lower the local elastic strain energy from deformation twins and stacking faults. This issue warrants further research that should include high resolution aberration

corrected analytical STEM and atomistic simulations which are not in the scope of the current study.

The experimental evidence of Suzuki segregation of molybdenum to stacking faults gives strong evidence that local chemistry changes in MP35N are responsible for the increase in yield strength observed when aged. For bulk samples of MP35N, the peak aged condition is reached by exposing the material to a temperature of 590°C for 4 hours [10] but fine wires drawn for use in the medical device industry experience elevated temperatures on the order of seconds before being air quenched to room temperature. The wires in this study were exposed to elevated temperatures for 60 seconds but in normal processing conditions, MP35N wires are exposed to high temperatures for times on the order of 10 seconds and similar magnitudes of strengthening are observed. From a standpoint of designing medical devices the changes in elastic and plastic properties cannot be ignored. The rotary beam fatigue test results shown in Figure 3.10 show how the increase in yield stress due to aging has a large effect on fatigue life as the material is aged. The diffusion controlled mechanism of Suzuki segregation may not be expected to be active on those short time scales. The thermodynamic driving force for preferred segregation of solute atoms is present but diffusion of substitutional elements such as Ni, Cr, and Mo is significantly slower compared to diffusion of interstitial elements, making the observed segregation of molybdenum atoms to stacking faults worthy of further discussion.

One of the main differences between fine wires used in medical devices and larger “bulk” MP35N samples used for plates, fasteners, or machined parts is the fine grain

size and heavily cold worked microstructure introduced to the wires following the drawing process. The electron micrographs of small diameter MP35N wires show the already fine grained material to contain numerous deformation twins that are separated by tens of nanometers. Deformation twins are known to be effective boundaries to dislocations and decrease the effective grain size of a material. Processes that use aggressive cold work to form metals such as rolling or cold drawing have been shown to increase the vacancy concentration in FCC metals by the non-conservative movement of thermal jogs [50]. MP35N is a low stacking fault energy FCC metal that is known to readily form deformation twins that nucleate from dissociated dislocations and faulted regions of the crystal [26, 51] as the material is cold worked. The intersection of deformation twins and subsequent dislocation cutting provides an additional mechanism for further vacancy formation [52]. While the volume fraction of vacancies in an FCC metal is typically low at room temperature, heavily cold working the material can result in vacancy concentrations 2-3 orders of magnitude higher than under equilibrium conditions [50]. This large non-equilibrium vacancy concentration could significantly improve the diffusion rate of solute atoms to stacking faults and twins over the short length scales reported in this research.

5 SUMMARY AND FUTURE WORK

The work presented in this study helped to expand the understanding of the processing-properties-performance-microstructure relationship of MP35N wires used in medical device applications. Mechanical testing on cold worked MP35N wires showed the material strength and elastic modulus increased following a brief aging treatment at elevated temperatures. The increase in mechanical and elastic properties was coupled with a decrease in ductility and strain at break. Samples of MP35N wire in the as-drawn condition were analyzed using EBSD to determine if microstructural changes such as phase transformations, grain size refinement, or different crystallographic textures were present in aged wires. No microstructural changes were observed using EBSD. Conventional TEM and diffraction analysis of cold worked and aged MP35N revealed a microstructure consisting of FCC grains, deformation twins, stacking faults, and dislocations. No second phases or unusual microstructural features were observed following the aging process. The lack of any resolvable microstructural changes in cold worked MP35N by the introduction of aging treatments suggested that changes in local chemistry could be occurring. Previous research on the secondary hardening mechanism of MP35N hypothesized the mechanism for the observed age hardening of MP35N was a result of Suzuki segregation. In this study EFTEM, HAADF-STEM imaging, and STEM-EDS were used to probe the chemistry of MP35N at and near microstructural defects such as twins and stacking faults. Results of the analytical STEM experiments showed stacking faults and deformation twin boundaries to be enriched in molybdenum and depleted of nickel and cobalt compared with the matrix and un-aged samples. These observations are consistent with the strengthening mechanism of dislocation locking resulting from Suzuki segregation. The rapid strengthening that is

observed following aging treatments on MP35N wires over time scales on the order of seconds was hypothesized to be a result of short range diffusion made possible by the non-equilibrium vacancy concentration created following heavy cold working and defamation twin formation. This mechanism is in agreement with the EDS scans showing local enrichment and depletion of alloying elements only a few nanometers away from the twins and faults.

The results reported in this paper give a more thorough understanding of the secondary hardening mechanism in heavily cold drawn and aged MP35N wires. The foundation set by the current work opens up possibilities for future research including aberration corrected HAADF-STEM imaging and high resolution analysis including monochromated EELS and EDS mapping to collect data on a wide variety of wire cold work and aging conditions. One material condition of particular interest combines high amounts of cold work and the peak ageing, which resulted in low ductility fractures. Further testing on single crystal specimens would help further our understanding of how individual grains deform as MP35N is processed at high temperatures and may elucidate the mechanism by which elastic modulus changes with aging. *In-situ* micro and nano pillar compression experiments could help us gain the fundamental insight needed to understand the transition in deformation mechanism from traditional slip to shear banding, at a matching volume to atomistic simulations of the same phenomena.

6 REFERENCES

1. Smith, G.D. 1967 US patent no. 3,356,542.
2. Company, L.S.S. *MP35N Alloy: Nickel-cobalt based alloy of the Multiphase alloy system*. Available from: http://www.latrobesteel.com/assets/documents/datasheets/MP35N_extended.pdf
3. Escalas, F., et al., *Biocompatibility of materials for total joint replacement.* Journal of Biomedical Materials Research, 1976. **10**(2): p. 175-195.
4. Altman, P.A., et al., *Rotary bending fatigue of coils and wires used in cardiac lead design.* Journal of Biomedical Materials Research, 1998. **43**(1): p. 21-37.
5. Schaffer, J., *A HIERARCHICAL INITIATION MECHANISM APPROACH TO MODELING FATIGUE LIFE VARIABILITY IN 35CO-35NI-20CR-10MO ALLOY MEDICAL GRADE FINE WIRE*. 2007, Purdue University.
6. Graham, A.H. and J.L. Youngblood, *Work strengthening by a deformation-induced phase transformation in "MP alloys".* Metallurgical and Materials Transactions B, 1970. **1**(2): p. 423-430.
7. Drapier, J., et al., *Hardening Mechanisms in Multiphase Alloy MP35N*. 1970: Cobalt. p. 171-186.
8. Raghavan, M., B.J. Berkowitz, and R.D. Kane, *A transmission electron microscopic investigation of phase transformations in MP35N.* Metallurgical and Materials Transactions A, 1980. **11**(1): p. 203-207.
9. Singh, R. and R. Doherty, *Strengthening in MULTIPHASE (MP35N) alloy: Part I. ambient temperature deformation and recrystallization.* Metallurgical Transactions A, 1992. **23**(1): p. 307-319.
10. Asgari, S., et al., *The secondary hardening phenomenon in strain-hardened MP35N alloy.* Acta Materialia, 1998. **46**(16): p. 5795-5806.
11. Suzuki, H., Sci. Rep. Res. Inst., 1952. **A4**.
12. Fisher, J., et al., eds. *Dislocations and Mechanical Properties of Crystals*. 1956.
13. Hirth, J.P. and J. Lothe, *Theory of Dislocations*. 1982: Krieger Publishing Company.
14. Ishmaku, A. and K. Han, *Deformation induced Nanostructure and texture in MP35N alloys.* Journal of Materials Science, 2004. **39**(16-17): p. 5417-5420.
15. OTOMO, et al., *Influence of Cold-Working and Subsequent Heat-Treatment on Young's Modulus and Strength of Co-Ni-Cr-Mo Alloy*. Vol. 51. 2010, Sendai, JAPON: Japan Institute of Metals. 8.
16. Cai, S., et al., *Effect of Cold Work and Aging on a Cobalt-Nickel Based Alloy*, in *Biomaterials Science: Processing, Properties and Applications III*. 2013, John Wiley & Sons, Inc. p. 19-28.
17. Vander Voort, G. ***Metallographic Specimen Preparation for Electron Backscattered Diffraction***.
18. *The Diffraction Pattern*. Available from: http://www.ebsd.com/index.php/component/content/article/83-ebsd-for-beginners/111-the-diffraction-pattern.
19. Sorensen, D., et al., *Investigation of secondary hardening in Co–35Ni–20Cr–10Mo alloy using analytical scanning transmission electron microscopy.* Acta Materialia, 2014. **63**(0): p. 63-72.
20. Li, B., D. Sorensen, and T. Steigauf. *Phase Transformation Study on MP35N Wire for Lead Conductor* in *Materials & Processes for Medical Devices*. 2011.

ASM International.
21. Hu, H., *Texture of Metals.* Texture, 1974. **1**(4): p. 233-258.
22. Schwartz, A.J., M. Kumar, and B.L. Adams, *Electron Backscatter Diffraction in Materials Science*. 2000: Kluwer Academic.
23. Li, B.Q. and T. Steigauf, *Texture and Anisotropy of MP35N Wire for Conduct Leads*, in *Applications of Texture Analysis*. 2008, John Wiley & Sons, Inc. p. 627-635.
24. Dieter, G.E., *Mechanical metallurgy*. 1976: McGraw-Hill.
25. Zlateva, G. and Z. Martinova, *Microstructure of Metals and Alloys: An Atlas of Transmission Electron Microscopy Images*. 2008: Taylor & Francis.
26. Mahajan, S. and G.Y. Chin, *Formation of deformation twins in f.c.c. crystals.* Acta Metallurgica, 1973. **21**(10): p. 1353-1363.
27. Chiba, A., X.G. Li, and M.S. Kim, *High work-hardening rate and deformation twinning of Co-Ni-based superalloy at elevated temperatures.* Philosophical Magazine A, 1999. **79**(7): p. 1533-1554.
28. Karaman, I., et al., *The deformation of low-stacking-fault-energy austenitic steels.* JOM, 2002. **54**(7): p. 31-37.
29. Asgari, S., et al., *Strain hardening regimes and microstructural evolution during large strain compression of low stacking fault energy fcc alloys that form deformation twins.* Metallurgical and Materials Transactions A, 1997. **28**(9): p. 1781-1795.
30. Kestenbach, H.J., *Electron diffraction analysis of thin twin or HCP plates in an FCC matrix.* Metallography, 1977. **10**(2): p. 189-199.
31. Rollett, A., F.J. Humphreys, and G.S. Rohrer, *Recrystallization and Related Annealing Phenomena*. 2004: Elsevier Science.
32. Ahn, C.C., *Transmission Electron Energy Loss Spectrometry in Materials Science and the EELS Atlas*. 2006: Wiley.
33. Ahn, C.C. and O.L. Krivanek, *EELS Atlas: A Reference Collection of Electron Energy Loss Spectra Covering All Stable Elements*. 1983: Gatan.
34. Pennycook, S.J. and P.D. Nellist, *Scanning Transmission Electron Microscopy: Imaging and Analysis*. 2011: Springer.
35. Hillyard, S. and J. Silcox, *Detector geometry, thermal diffuse scattering and strain effects in ADF STEM imaging.* Ultramicroscopy, 1995. **58**(1): p. 6-17.
36. Yu, Z., D.A. Muller, and J. Silcox, *Study of strain fields at a-Si/c-Si interface.* Journal of Applied Physics, 2004. **95**(7): p. 3362-3371.
37. Phillips, P.J., et al., *Atomic-resolution defect contrast in low angle annular dark-field STEM.* Ultramicroscopy, 2012. **116**(0): p. 47-55.
38. Mkhoyan, K.A., et al., *Effects of amorphous layers on ADF-STEM imaging.* Ultramicroscopy, 2008. **108**(8): p. 791-803.
39. Muller, D.A., et al., *Atomic-scale imaging of nanoengineered oxygen vacancy profiles in SrTiO3.* Nature, 2004. **430**(7000): p. 657-661.
40. Jeong, J.S., et al., *Observation of Electrically-Inactive Interstitials in Nb-Doped SrTiO3.* ACS Nano, 2013. **7**(5): p. 4487-4494.
41. Varschavsky, A. and E. Donoso, *Modelling the kinetics of solute segregation to partial dislocations in cold-rolled copper alloys.* Materials Letters, 1997. **31**(3–6): p. 239-245.
42. Yang, Z., et al., *Direct observation of dislocation dissociation and Suzuki segregation in a Mg–Zn–Y alloy by aberration-corrected scanning transmission electron microscopy.* Acta Materialia, 2013. **61**(1): p. 350-359.

43. Koizumi, Y., et al., *Suzuki segregation in Co–Ni-based superalloy at 973 K: An experimental and computational study by phase-field simulation.* Acta Materialia, 2012. **60**(6–7): p. 2901-2915.
44. Viswanathan, G.B., et al., *Segregation at Stacking Faults within the γ' Phase of Two Ni-Base Superalloys Following Intermediate Temperature Creep.* Scripta Materialia, (0).
45. Han, G.W., I.P. Jones, and R.E. Smallman, *Direct evidence for Suzuki segregation and Cottrell pinning in MP159 superalloy obtained by FEG(S)TEM/EDX.* Acta Materialia, 2003. **51**(10): p. 2731-2742.
46. Hamdi, F. and S. Asgari, *Evaluation of the Role of Deformation Twinning in Work Hardening Behavior of Face-Centered-Cubic Polycrystals.* Metallurgical and Materials Transactions A, 2008. **39**(2): p. 294-303.
47. Benito, J.A., et al., *Change of Young's modulus of cold-deformed pure iron in a tensile test.* Metallurgical and Materials Transactions A, 2005. **36**(12): p. 3317-3324.
48. Yu, N., A.A. Polycarpou, and A.J. Wagoner Johnson, *Measuring mechanical properties of fine-wire cross-sections used in medical devices.* Journal of Biomedical Materials Research Part B: Applied Biomaterials, 2004. **70B**(1): p. 106-113.
49. Fallen, C.T., et al., *Measuring the elastic properties of fine wire.* Journal of Biomedical Materials Research, 2001. **58**(6): p. 694-700.
50. Militzer, M., W.P. Sun, and J.J. Jonas, *Modelling the effect of deformation-induced vacancies on segregation and precipitation.* Acta Metallurgica et Materialia, 1994. **42**(1): p. 133-141.
51. Venables, J.A., *The nucleation and propagation of deformation twins.* Journal of Physics and Chemistry of Solids, 1964. **25**(7): p. 693-700.
52. Seeger, A., *Production of lattice vacancies in metals by deformation twinning.* Philosophical Magazine Letters, 2007. **87**(2): p. 95-102.